

## Cryo-EM in drug discovery: achievements, limitations and prospects

Jean-Paul Renaud<sup>1,2,3\*</sup>, Ashwin Chari<sup>4\*</sup>, Claudio Ciferri<sup>5\*</sup>, Wen-ti Liu<sup>1\*</sup>,  
Hervé-William Rémigy<sup>6\*</sup>, Holger Stark<sup>4\*</sup> and Christian Wiesmann<sup>7\*</sup>

**Abstract** | Cryo-electron microscopy (cryo-EM) of non-crystalline single particles is a biophysical technique that can be used to determine the structure of biological macromolecules and assemblies. Historically, its potential for application in drug discovery has been heavily limited by two issues: the minimum size of the structures it can be used to study and the resolution of the images. However, recent technological advances — including the development of direct electron detectors and more effective computational image analysis techniques — are revolutionizing the utility of cryo-EM, leading to a burst of high-resolution structures of large macromolecular assemblies. These advances have raised hopes that single-particle cryo-EM might soon become an important tool for drug discovery, particularly if they could enable structural determination for ‘intractable’ targets that are still not accessible to X-ray crystallographic analysis. This article describes the recent advances in the field and critically assesses their relevance for drug discovery as well as discussing at what stages of the drug discovery pipeline cryo-EM can be useful today and what to expect in the near future.

In 2017, the Nobel Prize for chemistry was awarded to Jacques Dubochet, Joachim Frank and Richard Henderson “for developing cryo-electron microscopy [cryo-EM] for the high-resolution structure determination of biomolecules in solution” — a reflection of the spectacular results that have been achieved in recent years with single-particle cryo-EM in structural biology. However, the beginnings of this technique are much older; the first transmission electron microscope was developed in 1931 by Max Knoll and Ernst Ruska, leading to the first breaking of the light microscope limit in 1933 (FIG. 1).

Electron microscopy (EM) was initially not believed to be useful for imaging biological samples for two fundamental reasons: first, it was considered impossible to image biological molecules in the high vacuum that is required to operate an electron microscope; and second, the interaction of electrons with matter is very strong, and the resulting beam damage was believed to readily destroy biological samples. So, for several decades, scientists were able to image biological samples only by making use of heavy-metal salt staining, which nevertheless contributed to morphological understanding in cell biology and virology, such as providing the first images of viruses with EM, obtained by Helmut Ruska and colleagues, including his brother Ernst<sup>1–3</sup>.

Then, in 1981, Jacques Dubochet and Alasdair McDowell made a breakthrough in imaging macromolecular complexes with EM — introducing the rapid cryo-cooling of individual molecules in a thin layer of vitrified water — that simultaneously solved the two fundamental problems noted above<sup>4–7</sup>. Vitrification not only leads to the macromolecules being embedded in a close-to-native environment but also protects them from dehydration by imaging them at a low temperature. The cooling itself also helps to reduce the damage caused by the electron beam.

Nevertheless, other challenges remained, including the low contrast and large amount of noise in cryo-EM images of vitrified macromolecules and how to make use of the image information to determine the underlying 3D structure of the imaged objects (see BOX 1 for a brief overview of the fundamentals of cryo-EM image formation). The use of computational image processing techniques, pioneered by Joachim Frank and Marin van Heel<sup>8–10</sup>, has since been instrumental in the quantitative understanding of noisy cryo-EM images. Computational averaging of multiple copies of the same view of the imaged macromolecular complex led to a considerable improvement in signal-to-noise ratio, and the averaged images of molecules represented the

<sup>1</sup>NovoAlx, Illkirch, France.

<sup>2</sup>RiboStruct, Ostwald, France.

<sup>3</sup>IGBMC, CNRS UMR7104/INSERM U1258/Université de Strasbourg, Illkirch, France.

<sup>4</sup>Max Planck Institute for Biophysical Chemistry, Göttingen, Germany.

<sup>5</sup>Genentech, South San Francisco, CA, USA.

<sup>6</sup>Thermo Fisher Scientific, Eindhoven, Netherlands.

<sup>7</sup>Novartis Institutes for BioMedical Research, Basel, Switzerland.

\*e-mail: [jpr@ribostruct.com](mailto:jpr@ribostruct.com);  
[ashwin.chari@mpibpc.mpg.de](mailto:ashwin.chari@mpibpc.mpg.de);  
[ciferri.claudio@gene.com](mailto:ciferri.claudio@gene.com);  
[wliu@novalex.com](mailto:wliu@novalex.com);  
[HRemigy@fei.com](mailto:HRemigy@fei.com);  
[holger.stark@mpibpc.mpg.de](mailto:holger.stark@mpibpc.mpg.de);  
[christian.wiesmann@novartis.com](mailto:christian.wiesmann@novartis.com)

doi:10.1038/nrd.2018.77

Published online 8 Jun 2018

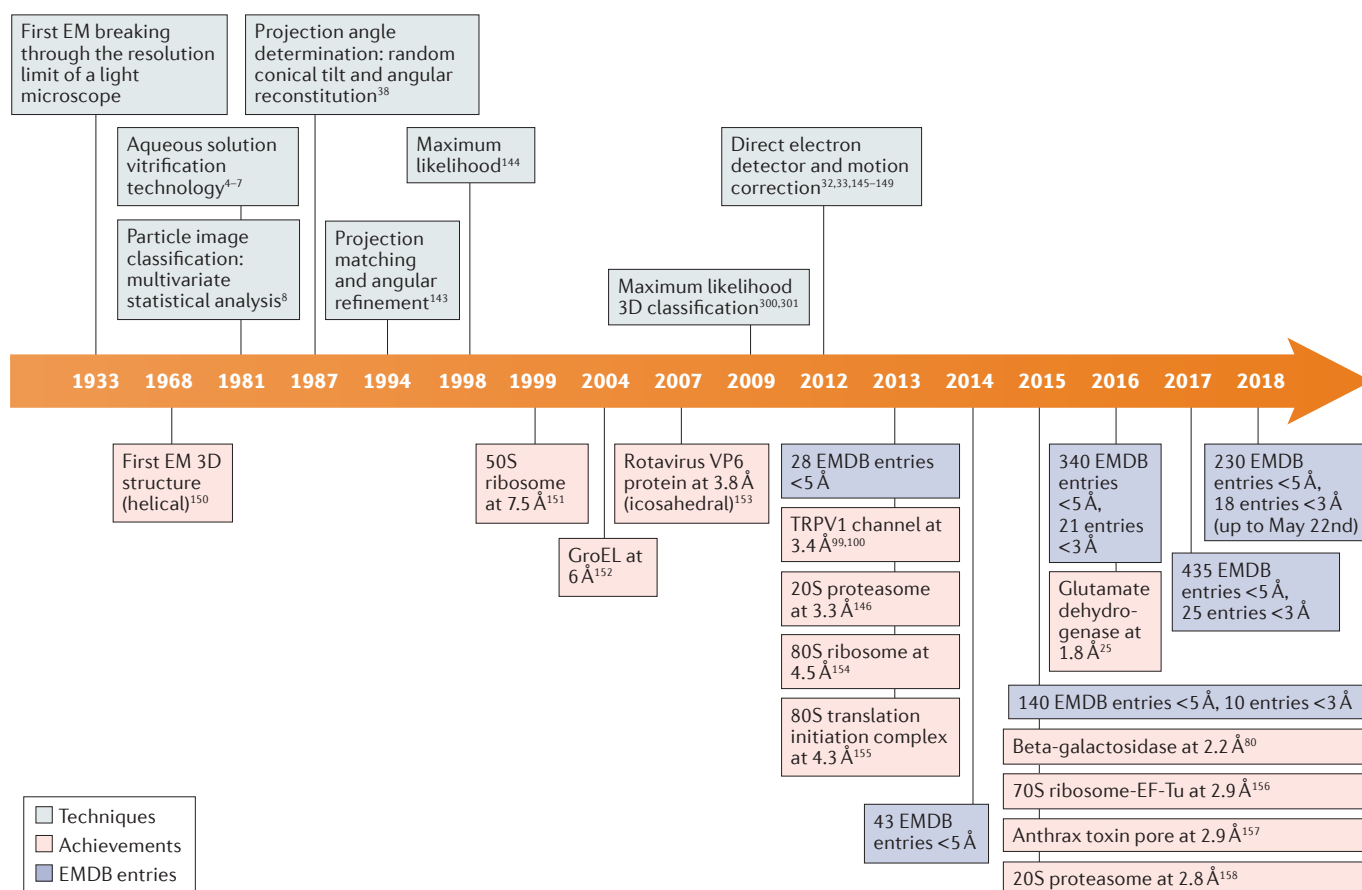


**Figure 1 | Cryo-EM timeline.** Selected key events in the development of single-particle electron microscopy (EM) are shown, with milestones in techniques shown in the upper part and structures solved shown on the lower part. The Electron Microscopy Data Bank (EMDB) entries listed in the lower part are specified only as single-particle method. TRPV1, transient receptor potential cation channel subfamily V member 1.

starting point for the development of the first tools to reconstruct their 3D structure (see FIG. 1 and references therein).

Numerous further developments in computational image processing have been made by many groups in the cryo-EM field (for examples, see references<sup>11-17</sup>), including the introduction of more user-friendly software (for examples, see references<sup>18-21</sup>) that harnesses the rapid growth in computational power in recent years. In parallel to these computational developments, the advent of direct electron detectors has improved the image quality to such an extent that it has become possible to determine the high-resolution 3D structures of well-behaved macromolecular complexes within a few days. Cryo-EM-based structure determination of macromolecular complexes has thus now become a method that can be used not only by specialists, which has led to numerous new cryo-EM laboratories being installed globally.

The combination of direct electron detectors attached to high-end electron microscopes that have been continually improved over decades in terms of their stability, optical quality and automation, as well as the advances in software and computational power,

are driving a resolution revolution in cryo-EM-based structure determination, leading to a rapidly growing number of published high-resolution structures<sup>22,23</sup>. Recently published cryo-EM structures (a selection of which is presented in TABLE 1) include not only a wealth of biologically important and diverse structures that could probably not have been analysed by X-ray crystallography — including large dynamic assemblies and membrane protein complexes — but also ever-smaller objects (the current reported limit being human haemoglobin (64 kDa)<sup>24</sup>) and structures at increasingly high resolution, including complexes with small molecules (the current reported limit being glutamate dehydrogenase (1.8 Å)<sup>25</sup>).

With these rapid advances, there has been a surge of interest in the potential for applying cryo-EM in drug discovery, for which the value of structural information derived from X-ray crystallography and NMR spectroscopy is now very well established<sup>26-29</sup>. Importantly, cryo-EM studies do not require crystallization of the sample, which is a clear advantage over crystallography when the dynamics of the target hamper crystallization. Furthermore, single-particle cryo-EM provides partial access to the system's dynamics by identifying

**Box 1 | Fundamentals of cryo-EM image formation**

Analogous to the way light microscopes exploit differences in the way the components of a specimen interact with visible light to form an image with contrast, electron microscopes exploit differences in the way electrons interact with the specimen components. The resolution of a microscope is limited by the wavelength of light or other waves interacting with the specimen. Consequently, electron microscopes can achieve a much better resolution than light microscopes because electrons (which behave as both particles and waves) can reach a much shorter wavelength than light by being accelerated through a high potential difference (for example, a wavelength of 0.0197 Å under 300 kV of accelerating voltage, compared with the 0.5 µm wavelength of green light). Similar to the lenses in a light microscope, which focus or disperse light, electrostatic and electromagnetic lens systems in electron microscopes are used to manipulate the electron beam in order to achieve image magnification.

Cryo-electron microscopy (cryo-EM) refers to transmission EM (TEM), in which an electron beam transmits through a specimen to form an image. Therefore, an electron micrograph can be considered as 3D information compressed into a 2D form at a certain projection angle. While the electron wave travels through the specimen, the electron wave is scattered by the specimen, resulting in different electron densities on the image plane. The electron density difference between two adjacent areas is called the contrast.

In TEM, there are two sources of contrast: amplitude contrast and phase contrast. Amplitude contrast is created when the electron is scattered at high angle or loses its energy, and this usually occurs when components of the specimen interact strongly with the electron. The biological samples studied by cryo-EM are composed of light atoms, which electrons do not interact strongly with; therefore, phase contrast is the main contrast source. Phase contrast is generated when an electron passing through a sample is scattered at a small angle, which alters the phase of the wave without changing the amplitude.

However, unlike amplitude contrast, phase contrast is not directly observable. To transform a phase contrast into a detectable intensity change, an additional phase shift of  $\pi/2$  needs to be introduced physically. This additional phase shift can be achieved by spherical aberration or defocus. Spherical aberration is a defect of the lens system, and defocus is an aberration to obtain an image out of focus that can be manually introduced and precisely adjusted. Phase plates, which have only recently been developed for cryo-EM compared with the classic defocus manipulation, serve the same purpose of introducing an additional phase shift.

The additional phase shift enables the detection of phase contrast, yet the detected contrast remains weak, as the contrast was originally generated from weak interactions between electrons and the sample. As biological samples are sensitive to radiation damage, the electron beam needs to be used at low dose for imaging, which also weakens sample–electron interactions. Moreover, owing to microscope imperfections, such as the electron beam incoherence and the aberration from the lens system, the detected contrast is further dampened, and this is unfortunately even more pronounced with the high-resolution information. Therefore, electron micrographs contain a mixture of weak informative signal and a large amount of noise and always require further processing.

individual conformational states. However, the resolution of cryo-EM is not sufficient to see the detailed chemical environment of the ligand at present, and as a general tool for drug screening, cryo-EM is much more inefficient than X-ray crystallography because of the longer data acquisition time and computational analysis required. As such, cryo-EM presently complements other structural biology techniques such as X-ray crystallography and NMR, with its strengths lying particularly in studying large structures of multi-megadalton size for which NMR imposes severe technical demands and for which crystallization is extremely difficult.

In this article, we describe the recent advances in the field of cryo-EM and critically assess their relevance for drug discovery. We also discuss at what stages of the drug discovery pipeline cryo-EM can be useful at present and what to expect in the near future.

**The cryo-EM process: state of the art**

To determine a structure by cryo-EM, several steps are involved: sample treatment, EM grid preparation, image acquisition and image processing (BOX 2). Technical improvements at all these steps in recent years are increasing the potential to apply cryo-EM in drug discovery, and three main aspects of these achievements will be highlighted and discussed in this section: obtaining higher-resolution cryo-EM maps, working on smaller proteins and increasing the throughput.

**Obtaining higher-resolution cryo-EM maps**

Reaching higher resolutions was clearly the first prerequisite for cryo-EM to play a role in small-molecule structure-based drug design (SBDD) because ligands have to be unambiguously identified and their conformation and interactions with the target macromolecule precisely visualized in the map. For X-ray crystallography, it is generally considered that a resolution of at least ~2.5 Å is needed to enable structural information to be applied effectively in drug design. The resolution limit of most cryo-EM maps was restricted to ~5 Å for many years, but recent technical improvements in image acquisition and image processing have enabled resolutions better than 3 Å to be obtained.

**Advances in transmission EM.** The various components of electron microscopes, including electron sources, the vacuum, sample holders, power supplies, optical lens systems and detectors, have been continuously improved over several decades. One important technical improvement was the introduction of field emission electron sources, which generate a much more brilliant and coherent electron beam than the traditional electron sources such as tungsten filaments and LaB<sub>6</sub> sources.

**Advances in detectors.** For image-recording media, the field has progressed slowly from photographic film to charge-coupled device (CCD) cameras to the

Table 1 | **Selected recent cryo-EM structures, divided into four categories**

Object	Reported resolution	Refs
<i>Large and/or dynamic assemblies</i>		
Yeast transcription initiation complex	3.6 Å	221
Human transcription initiation complex	3.9 Å	222
<i>Schizosaccharomyces pombe</i> mediator	4.4 Å	223
<i>Saccharomyces cerevisiae</i> pre-initiation complex	4.7 Å	224
<i>S. cerevisiae</i> pre-initiation complex—core mediator complex	5.8 Å	224
Yeast U4/U6.U5 tri-snRNP	3.7 Å	225
Human U4/U6.U5 tri-snRNP	7 Å	226
<i>S. pombe</i> spliceosome (mixture of complexes)	3.6 Å	227
<i>S. cerevisiae</i> pre-catalytic spliceosome (complex B)	3.7 Å	228
<i>S. cerevisiae</i> activated spliceosome (Bact complex)	3.5 Å	229
<i>S. cerevisiae</i> activated spliceosome (Bact complex)	5.8 Å	230
<i>S. cerevisiae</i> spliceosome immediately after branching (complex C)	3.8 Å	231
<i>S. cerevisiae</i> spliceosome immediately after branching (complex C)	3.4 Å	232
Human spliceosome just prior to exon ligation (complex C*)	3.8 Å	233
Human spliceosome just prior to exon ligation (complex C*)	5.9 Å	234
<i>S. cerevisiae</i> spliceosome just prior to exon ligation (complex C*)	4.0 Å	235
<i>S. cerevisiae</i> spliceosome just prior to exon ligation (complex C*)	3.8 Å	236
<i>S. cerevisiae</i> spliceosome immediately after exon ligation (complex P)	3.7 Å	237
<i>S. cerevisiae</i> spliceosome immediately after exon ligation (complex P)	3.3 Å	238
Zika virus	3.8 Å	239
Herpesvirus capsid	3.1 Å	240
Human actomyosin–tropomyosin complex	3.9 Å	241
Mouse mammary tumour virus intasome	5 Å	242
Porcine respiratory supercomplex SCI1III2IV1	4.0 Å	243
Human respiratory supercomplex SCI1III2IV1	3.9 Å	244
HIV-1 EnvΔCT in complex with the PGT151 Fab	4.2 Å	122
Natively glycosylated HIV-1 Env in complex with bnAbs	3.5 Å	245
Yeast proteasome lid	3.5 Å	246
Yeast 26S proteasome (two structures)	4.6–4.8 Å	247
Human 26S proteasome	3.5 Å	248
<i>Escherichia coli</i> 70S ribosome in complex with SelB and Sec-tRNA <sup>Sec</sup> (six intermediate structures)	3.4–5.3 Å	249
Human 80S ribosome	~3 Å	250
<i>S. cerevisiae</i> small-subunit processome	3.8 Å	251
<i>Chaetomium thermophilum</i> 90S pre-ribosome	3.2 Å	252
<i>S. cerevisiae</i> nucleolar pre-60S ribosomal subunit	3.4 Å	253
Microtubules in different nucleotide states	3.5 Å	254
HIV-1 strand transfer complex intasome	~3.5–4.5 Å	255
197 bp nucleosome in complex with linker histone H1.5DC50	6.2 Å	256
<i>E. coli</i> relaxase	3.9 Å	257
<i>Pseudomonas aeruginosa</i> CRISPR RNA-guided surveillance complex bound to AcrF1 and AcrF2	3.4 Å	258
<i>P. aeruginosa</i> CRISPR RNA-guided surveillance complex bound to target double-stranded DNA	2.9 Å	259
Late-stage assembly intermediates of the human mitoribosomal large subunit	~3 Å	260

Table 1 (cont.) | **Selected recent cryo-EM structures, divided into four categories**

Object	Reported resolution	Refs
<b>Large and/or dynamic assemblies (cont.)</b>		
<i>S. cerevisiae</i> cleavage and polyadenylation factor polymerase module	3.5 Å	261
Human cleavage and polyadenylation specificity factor core module bound to the PAS hexamer motif	3.1 Å	262
Dynein tail–dynactin–BICDR1 complex	3.5 Å	263
Polycomb repressive complex 2	4.6 Å	264
<i>S. cerevisiae</i> oligosaccharyltransferase complex	3.5 Å	265
GATOR1–RAG GTPase complex	4.0 Å	266
Activator-bound human translation initiation factor eIF2B	4.1 Å	267
Activator-bound human translation initiation factor eIF2B	2.8 Å	302
Insulin receptor extracellular domain–insulin 1:2 complex	4.3 Å	268
<b>Membrane protein complexes</b>		
Zebrafish $\alpha$ 1-glycine receptor in complex with strychnine, glycine and glycine and ivermectin	3.8–3.9 Å	105
GluK2 in its desensitized state	3.8 Å	269
Prokaryotic cobalt/magnesium transport protein CorA	3.8 Å	270
Mammalian voltage-gated calcium channel $\text{Ca}_v1.1$	3.6 Å	103
Mammalian voltage-gated potassium channel $\text{K}_v10.1$ (also known as EAG1 or KCNH1)	3.8 Å	271
Eukaryotic voltage-gated sodium channel $\text{Na}_v\text{PaS}$	3.8 Å	104
<i>Aplysia californica</i> $\text{Ca}^{2+}$ -activated $\text{K}^+$ channel	3.5 Å	272
<i>Caenorhabditis elegans</i> cyclic-nucleotide-gated channel bound to cGMP	3.5 Å	273
Human hyperpolarization-activated cyclic nucleotide-gated channel in the absence and presence of cAMP	3.5 Å	274
Serotonin receptor ( $5\text{-HT}_{3A}\text{R}$ )	4.3 Å	275
Zebrafish cystic fibrosis transmembrane conductance regulator	3.7 Å	276
Porcine respiratory supercomplex SCI1III2IV1	4.0 Å	243
Human respiratory supercomplex SCI1III2IV1	3.9 Å	244
Triheteromeric GluN1–GluN2A–GluN2B glutamate receptor ionotropic, <i>N</i> -methyl-D-aspartate in complex with a GluN2B-specific allosteric modulator	4.5 Å	277
Bovine MRP1 in presence and absence of leukotriene C4	3.3–3.5 Å	116
Human calcitonin receptor–salmon calcitonin–G protein heterotrimer	4.1 Å	111
Rabbit GLP1 receptor–human GLP1–G protein heterotrimer	4.1 Å	112
Human GLP1 receptor–G protein-biased peptide exendin P5–G protein heterotrimer	3.3 Å	113
Human adenosine $\text{A}_{2A}$ receptor–agonist–engineered G protein heterotrimer	4.5 Å	114
Voltage-gated potassium channel subunit $\text{K}_v11.1$ (also known as hERG1 or KCNH2)	3.8 Å	278
Human multidrug transporter ABCG2	3.8 Å	138
Human multidrug transporter ABCG2 bound to an inhibitor and two Fabs	3.1 Å	279
Type-1 ryanodine receptor in complex with immunophilin FKBP12 (also known as FKBP1A)	3.8 Å	109
Type-1 ryanodine receptor in multiple functional states	3.8–4.5 Å	110
Agonist-bound and antagonist-bound human TRPA1	3.9–4.7 Å	102
Human TRPML1 channel structures in open and closed conformations	3.5–3.7 Å	280
Mouse TRPML1 channel embedded in nanodiscs	3.6 Å	281
Common marmoset TRPML3 channel	2.9 Å	106
Human TRPM4 bound to $\text{Ca}^{2+}$ and a modulator	3.8 Å	282
Mouse TRPM4 in the ATP-bound and apo states	2.9–3.1 Å	107
Mammalian SUR1–inward rectifier $\text{K}^+$ channel Kir6.2 channel bound to glibenclamide and ATP	3.6 Å	283

Table 1 (cont.) | **Selected recent cryo-EM structures, divided into four categories**

Object	Reported resolution	Refs
<b>Membrane protein complexes (cont.)</b>		
Unliganded, agonist-bound and antagonist-bound rat TRPV1	2.9–3.4 Å	101
Rabbit TRPV2	~4 Å	284
<i>Xenopus tropicalis</i> TRPV4	3.8 Å	285
Rabbit TRPV5 in the presence of econazole	4.8 Å	286
Human PC2 (also known as PKD2) channel in lipid nanodiscs	3.0 Å	287
Nanodisc-reconstituted yeast vacuolar ATPase $V_o$ proton channel	3.5 Å	288
Mammalian voltage-dependent calcium channel TPC1 in the presence and absence of phosphatidylinositol 3,5-bisphosphate	3.2–3.4 Å	289
<i>Blastochloris viridis</i> light-harvesting 1–reaction centre (LH1–RC) complex	2.9 Å	290
<i>Flavobacterium johnsoniae</i> alternative complex III alone and in supercomplex with cytochrome c oxidase $aa_3$	3.6 Å	291
27-fold and 28-fold single-ring pores formed by the amino-terminal fragment of mouse gasdermin A3	3.8–4.2 Å	292
<b>Ever-smaller objects</b>		
Human peroxiredoxin 3 dodecamer (257 kDa)	4.4 Å	126
Nucleosome core particle (200 kDa)	3.9 Å	293
Human $\gamma$ -secretase (~170 kDa + 30–70 kDa from glycosylation)	3.4 Å	98
Human peptide transporter TAP in complex with the herpesvirus ICP47 protein (166 kDa)	6.5 Å	139
Human calcitonin receptor–salmon calcitonin–G protein heterotrimer (~150 kDa)	4.1 Å	111
Chicken heart lactate dehydrogenase B in complex with an inhibitor (145 kDa)	2.8 Å	25
Human isocitrate dehydrogenase 1 R132C in the absence and presence of an inhibitor (93 kDa)	3.8 Å	25
Human haemoglobin (64 kDa)	3.2 Å	24
<b>Objects at high resolution, including complexes with small molecules</b>		
<i>E. coli</i> 70S ribosome in complex with elongation factor Tu and kirromycin <sup>a</sup>	2.9 Å	156
<i>P. aeruginosa</i> CRISPR RNA-guided surveillance complex bound to target double-stranded DNA	2.9 Å	259
Common marmoset TRPML3 channel	2.9 Å	106
ATP-bound mouse TRPM4 <sup>b</sup>	2.9 Å	107
Agonist-bound rat TRPV1 <sup>b</sup>	2.9 Å	101
<i>B. viridis</i> light-harvesting 1–reaction centre (LH1–RC) complex	2.9 Å	290
Adeno-associated virus AAV-DJ (gene therapy vector) in complex with fondaparinux	2.8 Å	294
<i>Thermoplasma acidophilum</i> 20S proteasome	2.8 Å	158
Chicken heart lactate dehydrogenase B in complex with an inhibitor	2.8 Å	25
Rabbit muscle aldolase <sup>c</sup>	2.6 Å	97
<i>Leishmania donovani</i> ribosome in complex with paromomycin	2.5–2.7 Å	295
<i>Trypanosoma cruzi</i> ribosome large subunit	2.5 Å	296,297
<i>T. acidophilum</i> 20S proteasome <sup>d</sup>	2.4 Å	50
Human AAA* ATPase p97 in presence and absence of an allosteric inhibitor	2.3–2.4 Å	298
Rhinovirus B14 in complex with the C5 Fab	2.3 Å	299
$\beta$ -Galactosidase in complex with a cell-permeant inhibitor	2.2 Å	80
Bovine glutamate dehydrogenase <sup>e</sup>	1.8 Å	25

AAA\*, ATPases associated with diverse cellular activities; ABCG2, ATP-binding cassette subfamily G member 2; AcrF1 and AcrF2, efflux pump membrane transporters; BICDR1, bicaudal D-related protein 1 (also known as BICDL1); bnAbs, broadly neutralizing antibodies; Env, envelope glycoprotein gp160; Fab, antigen-binding fragment; GLP1, glucagon-like peptide 1; MRP1, multidrug resistance-associated protein 1; PAS, polyadenylation signal; PC2, polycystin 2; SelB, selenocysteine-specific elongation factor; snRNP, small nuclear ribonucleoprotein particle; SUR1, sulfonylurea receptor 1 (also known as ABCC8); TAP, tip-associated protein; TRP, transient receptor potential cation channel. <sup>a</sup>Spherical aberration (Cs)-corrected cryo-EM to obtain a near-uniform resolution. <sup>b</sup>Using nanodiscs. <sup>c</sup>Using a 200 keV microscope. <sup>d</sup>Data acquisition using a Volta phase plate with defocus enabling contrast transfer function measurement and correction. <sup>e</sup>Highest resolution claimed using cryo-EM so far.



## Box 2 | Single-particle cryo-EM workflow

Several steps are involved in determining molecular structures using cryo-electron microscopy (cryo-EM), as shown in the figure: sample treatment (panel a), EM grid preparation (panel b), image acquisition (panel c) and image processing (panel d).

### Sample treatment

The sample needs to be optimized for the subsequent EM grid preparation. The main goal is to preserve the intactness and to reduce the heterogeneity of the molecules while not reducing the image contrast later. Sample molecules can be stabilized by optimizing the buffer conditions and can be further strengthened by increasing intramolecular interactions with crosslinking methods such as GraFix<sup>55</sup>. Crowding agents such as glycerol or sugar result in a strong image background of the cryo-EM sample and should be removed, which can be achieved, for example, with a buffer exchange column. For membrane proteins, the transmembrane domain is usually stabilized by amphipols, weak detergents or nanodiscs.

### EM grid preparation

Two common ways are used for embedding biological molecules on a sample grid. In negative staining, molecules are embedded in a layer of heavy-metal salt solution, and, when dried, the heavy-metal salt surrounds the molecules. In cryo-sample preparation, the sample solution is deposited on the sample grid, excess sample solution is blotted away in order to achieve optimal ice thickness and the sample grid is then rapidly plunged into liquid ethane. The molecules are embedded in amorphous ice generated by flash cooling, a process called vitrification.

### Image acquisition

The sample grid is inserted into a transmission electron microscope and an image (or an image data set) is collected.

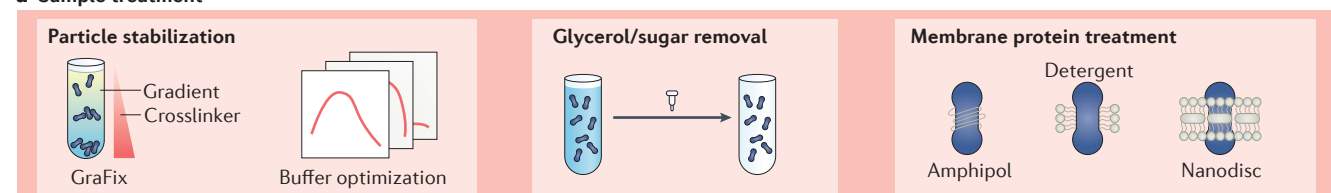
### Image processing

To reconstruct a 3D model, image processing is performed on the recorded data set of electron micrographs. To compensate for the low signal-to-noise ratio of the images, and especially for restoring the weak information at high resolution, the image processing procedure is based on the single-particle approach. 2D projections of the sample molecules — so-called particles — are visualized on the electron micrographs. These particles are selected separately as single images. Particle images representing the same view are then gathered into one group, and the images within the same group are averaged. With this process, the real signal is enhanced, whereas the random noise is reduced; hence, the signal-to-noise ratio of the images can be improved.

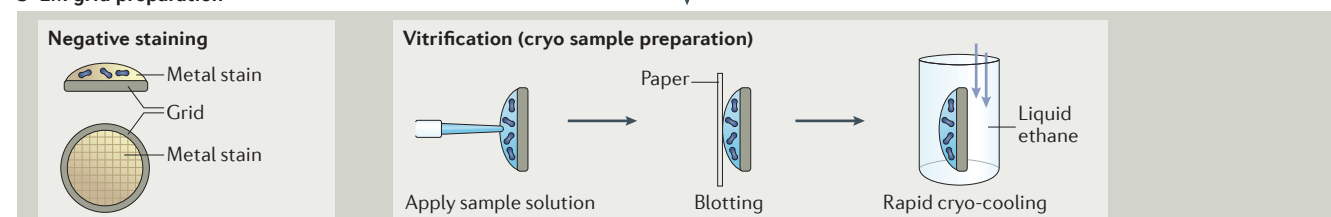
The angular relationship of these images is then obtained, either entirely by *in silico* computation (angular reconstitution) or using predefined information during image acquisition (random conical tilt). With the angular information, these images can then be back-projected to reconstruct a 3D model.

As cryo-EM captures the native state of the molecules, particles representing different conformations or different structures can be found in the same data set. 3D classification can be applied to resolve such heterogeneities. These states can be extracted separately, and then refinement can be applied to further improve the resolution.

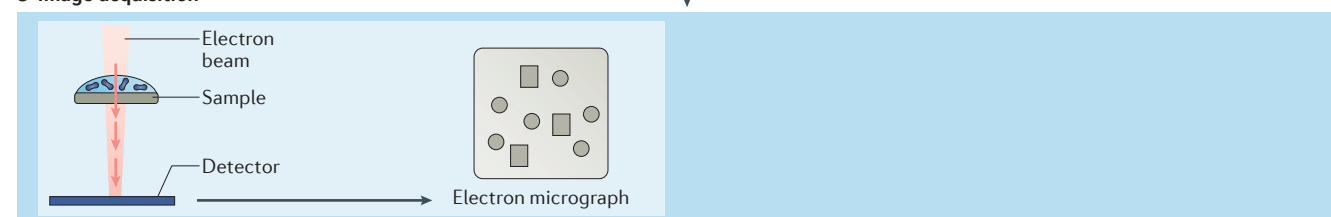
### a Sample treatment



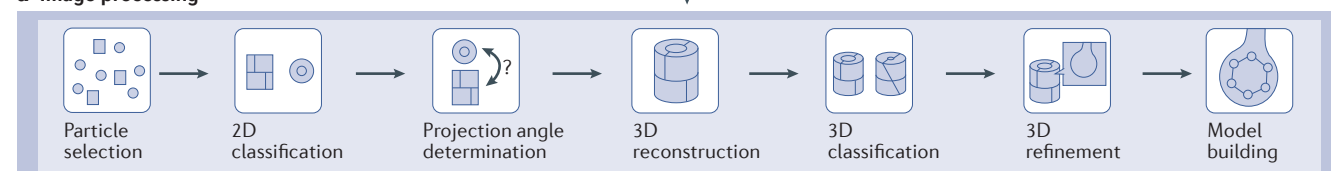
### b EM grid preparation



### c Image acquisition



### d Image processing



direct electron detectors used now. With direct electron detectors, images are usually recorded as stacks of ‘movie frames’ (typically several tens of frames) rather than an integrated total image. By following the particles from one frame to another, it is now possible to computationally compensate for image blurring<sup>30,31</sup>, which may be the result of stage drift, beam-induced particle motion and charging<sup>32,33</sup>. The alignment of frames minimizes the blurring of particle images and thus restores high-resolution information that was previously lost in blurred integrated images<sup>30,31</sup>.

Nevertheless, it is desirable to have as little motion as possible in the images. In recent publications, the use of graphene and gold EM grids was demonstrated to help substantially reduce image blurring<sup>34,35</sup>. It is interesting to note that the most dramatic blurring effects occur within the first three to five electrons per Å<sup>2</sup>. Usually, this cannot be corrected for efficiently by computational means and so these electrons are currently discarded from analysis. However, exactly those electrons potentially carry the highest-quality image information because they carry the signal that is almost free of beam damage<sup>36</sup>. Further development of optimal grid supports, in combination with image frame processing, will hopefully provide access to these most valuable parts of the images in the future, which could be essential in pushing the resolution limits of cryo-EM structures even further.

Improvements in image quality can also be obtained by running a direct detector in electron counting mode, where the electron dose in each image frame is sufficiently low to detect single-electron events on the detector. Stacks of thousands of such frames are needed to generate the final image. Currently, the speed of this image recording mode is slower than the conventional integration mode and is strongly dependent on the frame rate of the detector, which will improve in next-generation cameras. One of the advantages of electron counting is the enhancement of low spatial frequency information, resulting in an increased image contrast that is very beneficial for visualization of smaller macromolecular complexes. Counting mode may also be used for generating super-resolution images by trying to localize the detector event in a smaller region of the original pixel. Super-resolution capabilities will also become increasingly important in the design of chips for future detectors on the way to the development of the ‘perfect’ detector, which would be obtained when the detection quantum efficiency (DQE) gets close to 1 over the entire spatial frequency range.

Notably, the considerably improved signal-to-noise ratio of direct electron detectors does not directly improve the theoretical highest resolution achievable, but it reduces the number of images required to calculate a high-resolution structure. Indeed, an image data set recorded in a reasonable amount of time can be sorted into sub-data sets representing subtly different structural conformations, still with a sufficient number of particles to enable high-resolution 3D reconstruction; hence, the resolution can be improved. Addressing structural heterogeneity computationally is discussed further below.

**Advances in image processing.** The general workflow of image processing is described in BOX 2. With constant improvement of software algorithms and computational hardware utilization, image processing has been aiming at delivering high-resolution 3D structures in the most efficient way.

As noted above, modern direct electron detectors have enabled the preservation of high-resolution information in single movie frames. Image processing techniques have optimized the restoration of high-resolution information from the movie stack, resulting in output images used for further processing, and image blurriness can be reduced by aligning single frames. To further increase the precision of movie alignment, an image can be divided into patches, with every patch in each frame being aligned independently<sup>33</sup>. In addition, as high-resolution information decays with exposure time, the later frames of an image movie do not contribute much to the high-resolution information but still provide low-resolution information that can improve the overall image contrast. Fine manipulation of the contribution of each frame by applying filters (dose weighting) is useful for optimizing the content of high-resolution signals in a well-contrasted image<sup>37</sup>.

An EM image can be considered as 3D information compressed into a 2D form at a certain projection angle (BOX 1). Obtaining the angular information for initial 3D model reconstruction has been the most critical and the most challenging task for an unknown sample. Conventionally, the random conical tilt method has been widely used for this purpose<sup>38</sup>. However, after the conical tilt experiment has confirmed the angular information, an additional data set without sample tilting has to be collected for high-resolution reconstruction. Various algorithms and software packages have been developed to calculate angular information from a normal data set that can be used for later high-resolution 3D reconstruction, such as FREALIGN<sup>39</sup>, e2initialmodel module in EMAN2 (REF. 19), cryoSPARC<sup>20</sup> and SIMPLE<sup>40</sup>.

Resolving various 3D structures computationally from a single data set is not only beneficial for improving the resolution but also is helpful for understanding the structural variation of a macromolecule in its native state. The development and improvement of 3D classification algorithms, with less human interaction required and better precision, have now made it almost a routine step in the general image processing workflow<sup>41</sup>. 3D models of each class represent distinct structural states, and because each of them contains reduced intraclass heterogeneity, it is easier to be refined to higher resolution. Moreover, recently developed focused classification methods<sup>42–44</sup> have helped to resolve local heterogeneity and could be beneficial for distinguishing the protein particles with or without drug bound.

Recent developments with automatic image recording (which are discussed in the section on increasing throughput below), together with the movie form of recorded images, have considerably increased the amount of image information to be processed. These large image data sets can be handled by software that



uses graphics processing unit (GPU) processing<sup>18,45</sup> or runs on high-end central processing unit (CPU)-based workstations<sup>21</sup>.

### **Working on smaller proteins**

Cryo-EM has long been considered as a method mostly for macromolecules with molecular mass >500 kDa because the poor contrast transfer function achieved in highly defocused images made structural analysis of smaller complexes by cryo-EM challenging until recently<sup>46</sup>. However, many drug targets are small proteins and protein complexes, including membrane proteins. Importantly, the size limit of single-particle cryo-EM has been considerably lowered down to ~65 kDa in recent years<sup>24</sup> by the application of energy filters and Volta phase plates — two complementary technologies<sup>47</sup> that can both enhance the image contrast for small protein complexes.

Energy filters are operated in zero-loss mode, removing all electrons that have lost some energy while interacting with the sample (that is, electrons that are inelastically scattered and deposit energy in the sample). Such electrons do not contribute to the signal in EM images but contribute only to the noise, and their removal results in improved image contrast. However, the benefit of energy filtering becomes greater as sample thickness increases because more electrons are inelastically scattered; therefore, energy filtering is less beneficial for samples with smaller proteins embedded in very thin ice layers.

The idea of converting the image phase contrast into a detectable intensity difference goes back to the invention of phase plates in light microscopy<sup>48</sup>, where the phases of the unscattered and the scattered beam need to be shifted by  $\pi/2$  to obtain a substantial boost in image contrast. In EM, numerous ideas for phase plates have been explored so far, with the most recent success in high-resolution structure determination using the Volta phase plate system<sup>49–51</sup>, which can increase the image contrast to such an extent that haemoglobin (molecular mass = 64 kDa) became accessible to structure determination at 3.2 Å resolution<sup>24</sup>.

An alternative approach to overcome the size limitation is to form a rigid complex between the protein of interest and a monoclonal antigen-binding fragment (Fab) in order not only to increase the effective mass but also to facilitate image alignment<sup>52</sup>. Along the same lines, a recently described protein scaffold designed to self-assemble into a cubic cage was used to visualize a designed ankyrin repeat protein (DARPin; molecular mass = 17 kDa) attached to the scaffold using single-particle cryo-EM with a local resolution in the 3.5–5 Å range<sup>53</sup>. A potential advantage is that DARPins can be genetically engineered to exhibit high-affinity specific binding to various target proteins, broadening the range of application of this scaffolding system.

### **Increasing the throughput**

In addition to the quality requirement of high-resolution 3D reconstruction, throughput is also a crucial issue for drug discovery, as small-molecule SBDD relies on the

capacity to solve not just one or a few compound–target complexes but many. Several aspects of the cryo-EM process have been optimized to help increase throughput in recent years, including sample preparation, EM grid preparation, automated data collection and automated model building and structure refinement.

**Optimized sample preparation.** Although it is possible to resolve cryo-EM sample heterogeneity computationally, processing an image data set that contains broken particles and/or has extremely high heterogeneity is very time consuming and resource consuming, and allows for high-resolution structure determination of only the most rigid parts while losing structural information on the more mobile parts. The final resolution is also likely to be suboptimal. Therefore, the main goal for sample preparation is to preserve the intactness and to reduce the heterogeneity of the sample while not reducing the image contrast later.

The treatment of macromolecular complexes during purification and EM grid preparation plays an important role in the maximum achievable resolution for cryo-EM structures, especially for fragile and/or transient macromolecular complexes (for fragile samples, chemical fixation is also commonly applied; a mild chemical crosslinker is added to the sample in order to strengthen the particles through the formation of additional intramolecule interactions). There are two key parameters when optimizing the stability of macromolecular complexes for cryo-EM. First, the stability of multisubunit specimens is strongly influenced by the buffering conditions in which they are purified. Second, many macromolecular complexes require osmolytes such as glycerol or sucrose in order to be stabilized, but these additives are incompatible with cryo-EM grid preparation. These two issues in cryo-EM grid preparation can be addressed with two fairly recently developed techniques — ProteoPlex and GraFix<sup>54,55</sup>. ProteoPlex, an adaptation of the differential scanning fluorimetry (DSF) technique<sup>56,57</sup>, systematically explores stabilizing buffer conditions by using a sparse-matrix approach. An important advantage of ProteoPlex in comparison to DSF is that the method allows not only for screening of small-molecule stabilizers but also for screening of proteinaceous cofactors and binders such as nanobodies. ProteoPlex provides good guidance to biochemists; it can sample hundreds of conditions in the time required to screen one sample by EM, although the most promising conditions remain to be confirmed by EM imaging. GraFix is a density gradient centrifugation procedure that combines size fractionation and mild chemical fixation of macromolecular complexes. GraFix favours the formation of intramolecular links as the sample gradually encounters an increasing concentration of chemical fixative, in contrast to intermolecular crosslinks that often occur during the conventional batch fixation. GraFix also largely prevents dissociation of complexes under the optimal conditions for EM grid preparation, including fairly low (<0.1 mg ml<sup>-1</sup>) macromolecular complex concentrations and absence of osmolytes.

To perform structural analysis by cryo-EM, thousands of particles with various orientations are required. If the concentration of the biomolecule of interest is an issue, the use of functionalized (affinity) grids<sup>58–61</sup> or continuous film to concentrate the molecule<sup>62–64</sup> or reconcentration procedures that use multiple rounds of sample application and blotting<sup>65</sup> will become common practice.

**Optimized EM grid preparation.** After obtaining an optimized sample, it is transferred to an EM grid (BOX 2). Optimizing the preparation of EM grids is crucial for preserving particles in their native state and consequently increasing the ratio between ‘good’ and ‘bad’ particles. There are two main techniques for preparing purified macromolecular complexes for EM imaging that protect the molecules from the high vacuum in the microscope. The first technique is classical negative-stain imaging, which is valuable in obtaining initial 2D and 3D structural information about a given complex and extremely helpful for quality control during sample optimization. The second technique is based on vitrified aqueous solutions prepared by cryo-cooling, and cryo-samples are now used for all high-resolution structure determinations of macromolecular complexes.

In classical negative staining, molecules are typically embedded in a layer of heavy-metal salt solution, such as uranyl acetate. In general, the resolution from negative staining is limited to ~15 Å (although higher resolutions can be obtained by using cryo-negative staining<sup>66</sup>, in which the heavy-metal salt-treated grid is not dried but rapidly cooled and imaged under cryogenic conditions in the electron microscope). At present, negative staining is commonly used to observe the sample in the electron microscope at room temperature, as screening the specific physicochemical properties and preparation conditions (homogeneity, concentration and distribution) potentially suitable for obtaining a high-resolution structure can help increase analytical throughput. Although this is still a slow procedure, efforts have been initiated to overcome this bottleneck through EM automation<sup>14,15,20,67–69</sup> (see also EPU and JADAS in Related links), and improvements are expected.

Vitrified aqueous solutions are prepared by flash cooling the EM grid on which the sample is deposited in a cryogenic fluid, which prevents crystalline ice formation<sup>4</sup>. This method requires optimization of the sample concentration, the relative humidity rate, the hydrophilicity of the film placed on the grid (by plasma glow discharging), the nature of the grid itself (which can be made of copper or gold), the blotting force and the blotting time. The accurate quantification and the normalization of these parameters is important in reliably reproducing the sample vitrification process.

The vitrification process can be broken down into three steps: sample deposition, removal of sample excess to obtain a thin film and vitrification in a cryogenic fluid. For sample deposition, application of the sample on a holey film followed by the blotting of the sample excess using Whatman paper type 1 has been used for more than three decades<sup>7</sup> and is still the most

popular method<sup>70</sup>. The need to vary sample preparation conditions and increase the throughput motivated pioneering groups to develop spotting technologies, in which volumes ranging from the nanolitre to the picolitre are effectively deposited<sup>71–73</sup>. To analyse the structural dynamics of target–ligand interactions, methods have been developed to characterize transient functional states by time-resolved cryo-EM: just before its deposition on the grid, the solution containing the macromolecule of interest is rapidly mixed with a solution containing a ligand using mixing–spraying devices<sup>71,74–76</sup>. The main limitation of this methodology is the need to obtain a surface comprising targets interacting with their ligand that is large enough to collect a data set of sufficient size to identify enough transient conformations to understand the underlying mechanism. A recent module that has an internal mixing system made of polydimethylsiloxane that could be connected or integrated in the future to various fluidic devices could change that paradigm<sup>73</sup>. Another notable recent technical advance, pioneered by Braun and colleagues<sup>77</sup>, is spreading a thin sample film using micro-capillaries and direct ‘plunge freezing’ in liquid ethane. Although such blotless technologies are currently being developed, traditional sample blotting is still the most popular approach to obtain a thin film to reduce the electron scattering due to ice.

The second step — obtaining the optimal ice thickness for a given sample by removing excess sample — has a key role in obtaining a near-atomic structure of a complex. Most macromolecular complexes have a size range of 10–100 nm, which is smaller than the mean free path lengths of 300 kV electrons<sup>78</sup>, making such complexes ideally suited for cryo-EM studies. However, the vitrified water layer should be only slightly thicker than the molecules to obtain the best possible signal quality and contrast<sup>79,80</sup> while displaying a variety of orientations of the object of interest to allow its 3D reconstruction from a variety of projections. This step is the most difficult to reproduce and still needs attention from cryo-EM method developers. Nevertheless, sample spreading techniques are maturing<sup>72</sup>. Glaeser and colleagues developed a technique using a thin surfactant layer when preparing cryo-EM grids to improve the sample thickness reproducibility before vitrification<sup>81</sup>. Self-blotting grids containing nanowires<sup>72</sup> have also been developed to streamline the cryo-sample preparation process and increase its throughput, which remains low in comparison with cryo-preparation of 3D crystals for X-ray crystallography, for example.

After sample deposition and before fast vitrification, the particles on the grid can adopt a preferred orientation. This is a common problem<sup>82</sup>, especially when the grid is covered with a continuous film (in general a carbon film) on which the particles settle. This phenomenon also occurs with holey films (where particles ‘float’ in the disc of water inside micrometric holes), and they frequently concentrate at the water–air interface, where they are prone to denaturation and aggregation (see REFS 47,83 for discussion of the relative merits of continuous and holey films). Efforts are ongoing to

solve this issue, for example, by employing tilts during data collection<sup>84</sup> to obtain an isotropic distribution of angular projection orientations to recover the loss of information in the Fourier space resulting from preferred orientation.

Since the beginning of cryo-EM, the third step of grid vitrification has been performed by vertically plunging the EM grid into the cryogenic coolant — either ethane or an ethane–propane mixture cooled to around  $-170$  to  $-180$  °C using liquid nitrogen. Initially, grids were vitrified manually using tweezers, but cryo-plungers have been built to improve reproducibility, principally to reduce artefacts related to evaporation<sup>85</sup>. These devices limit the interaction between the sample thin film layer and its environment after the blotting step and before the vitrification step<sup>86,87</sup>, and currently vitrification is greatly facilitated by several commercially available robotic ‘plunge-freezing’ machines<sup>88,89</sup>.

The effect of the grid geometry during its penetration into the coolant suggested that a horizontal plunging of the grid — with the grid bent to be parallel to the cooling bath<sup>90</sup> — could drastically increase the cooling rate of the thin film and thereby avoid the formation of crystalline ice resulting from insufficiently rapid vitrification. These new methodologies will allow for more systematic cryo-sample preparation screening and enable grids perfectly suited for the acquisition of high-resolution data sets to be obtained. In a recent paper suggesting that most particles inevitably bind and eventually aggregate at the water–air interface, Noble and colleagues advocate for the use of cryo-electron tomography to inspect the sample (ice thickness, particle distribution and orientation) and to optimize it before acquiring a data set aiming at high-resolution 3D reconstruction<sup>91</sup>.

**Automated data collection systems.** With recently developed software packages, such as Legicon<sup>14</sup>, SerialEM<sup>15</sup> and EPU (see Related links), multiple electron micrographs can be collected automatically from a user-selected area on a sample grid. Advances in hardware have also facilitated image acquisition automation. Grid transferring is automated with robotic sample loading. Use of CCD cameras previously, or of direct electron detectors at present, also fits well with the automation scheme as breaking the microscope vacuum in order to exchange the photographic film plates is no longer needed. As another advantage, the signal-to-noise ratio of direct electron detectors is considerably improved; therefore, the number of images required for calculating a high-resolution structure is reduced.

**Automated model building and structure refinement.** Since the advent of high-resolution cryo-EM structures, software and protocols adapted to near-atomic data have been developed to automate model building<sup>92,93</sup> and structure refinement<sup>94,95</sup>. A procedure for reference-based local sharpening of cryo-EM density maps was also described recently and was shown to facilitate model building and structure refinement<sup>96</sup>.

**Development of simpler microscopes.** Even if data collection algorithms and camera speed are improved, the overall speed of data collection for typical drug discovery projects would not be dramatically better than at present because of the need to study multiple structures (for example, with different ligands). The only way to achieve a similar throughput to that of crystallography at present would be to have several Titan Krios microscopes in a single location for data collection, but this would be prohibitively costly. Given this, there is an impetus for the development of simpler microscopes, and constructors have recently started to offer more compact systems than the Titan Krios (such as the Thermo Fisher Scientific Glacios; see Related links) but with the same automated sample-handling capabilities. More compact systems enable pre-screening at lower cost to select the best grid candidates to be transferred to a Titan Krios microscope to acquire the best data sets possible. Although not as powerful, such more affordable systems are also capable of reaching beyond 3 Å structure resolution<sup>97</sup>.

### Applications in drug discovery

Structural biology can be useful at all stages of preclinical target-based drug discovery, including target identification and validation, hit generation, hit-to-lead and lead optimization, provided the structure of the target can be solved. FIGURE 2 shows the history of the adoption of the main biophysical methodologies for 3D structure determination of macromolecules — X-ray crystallography, NMR and cryo-EM — in drug discovery. Briefly, the main advantages of the three methods are the following. X-ray crystallography can rapidly and reproducibly yield high-resolution structures when the target is amenable to crystallization and once a robust system has been set up. NMR allows fast hit identification and triage and provides information on the system's dynamics. Cryo-EM allows structure determination of large and/or dynamic macromolecular assemblies in solution without the need to obtain crystals and, even more importantly, in their native state, including post-translational modifications; moreover, different conformational states can be resolved in one experiment. A more detailed comparison of cryo-EM and X-ray crystallography in drug discovery is provided in BOXES 3,4.

Cryo-EM has already demonstrated its usefulness in target identification, validation and characterization, which typically involves target structure analysis to understand the mechanism of action and assess druggability. This analysis requires access to the native structure, ideally in complex with biological partners. Since the 1990s, cryo-EM has been used in combination with X-ray crystallography to solve the structure of large assemblies that were not amenable to crystallization. Low-resolution molecular envelopes obtained from the contouring of the EM density map (by using a threshold related to the molecular mass of the object to remove the voxels corresponding to noise) can provide an approximate contour of the object into which high-resolution crystal structures of domains, individual proteins or subcomplexes can be fitted.

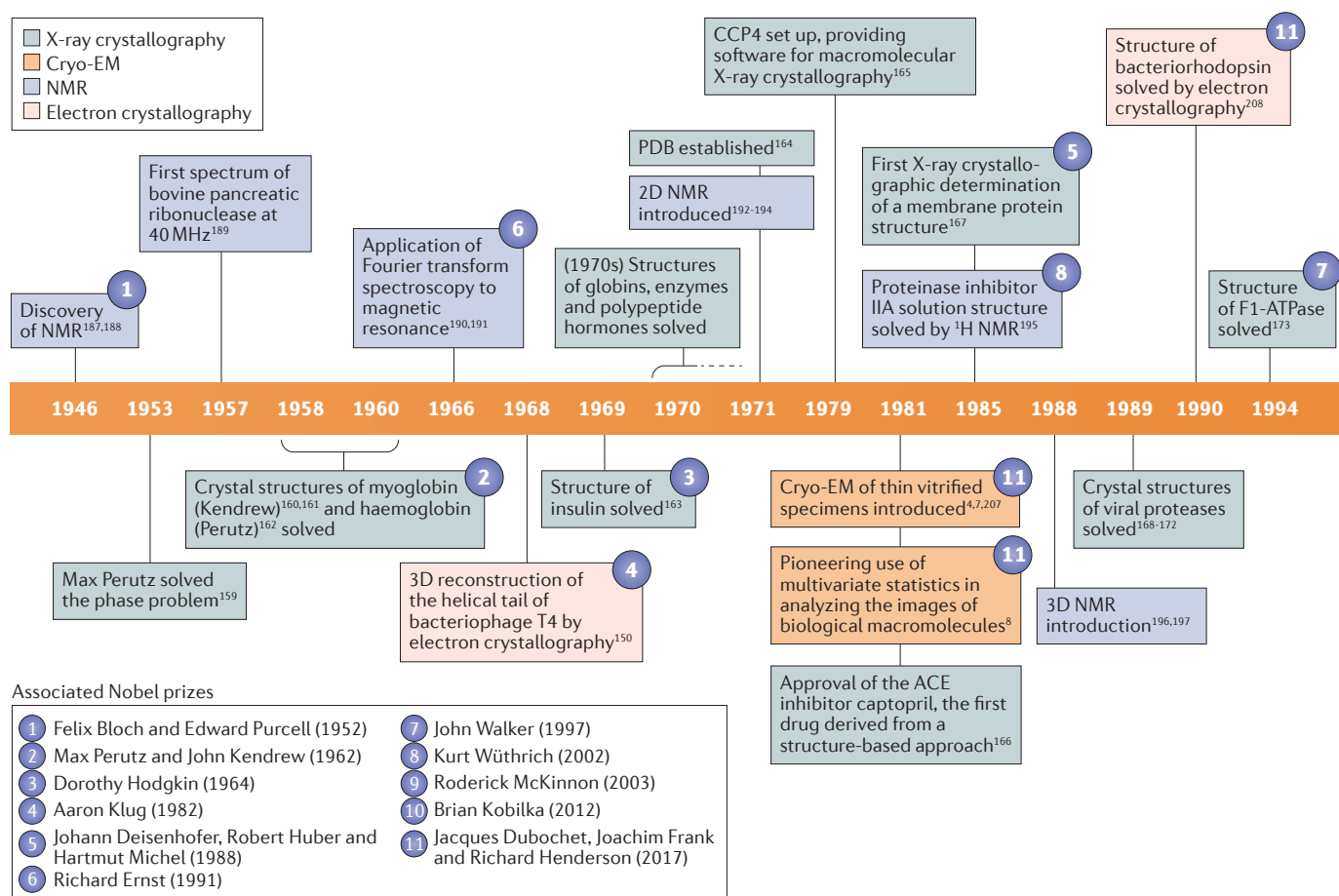


**Figure 2 | Selected key events in the development of the three main biophysical methodologies for 3D structure determination of macromolecules for drug discovery.** Events for X-ray crystallography are shown in green, events for nuclear magnetic resonance (NMR) are shown in blue and events for cryo-electron microscopy (cryo-EM) are shown in orange. Electron crystallography achievements using bidimensional crystals of proteins are in light pink; although the use of this technique declined as single-particle analysis (SPA) became the most common technique, its use indicates the potential of electron microscopes for near-atomic structure

determination in life sciences. Nobel Prize winners linked in part to the selected events are indicated using numbers, with the years of the award in parentheses. ACE, angiotensin-converting enzyme; CCP4, Collaborative Computational Project number 4; CCP-EM, Collaborative Computational Project for Electron Microscopy; EMBD, Electron Microscopy Data Bank; FAXS, fluorine chemical shift anisotropy and exchange for screening; FBDD, fragment-based drug discovery; GPCR, G protein-coupled receptor; PDB, Protein Data Bank; SAR, structure-activity relationships; SBDD, structure-based drug design; STD, saturation transfer difference.

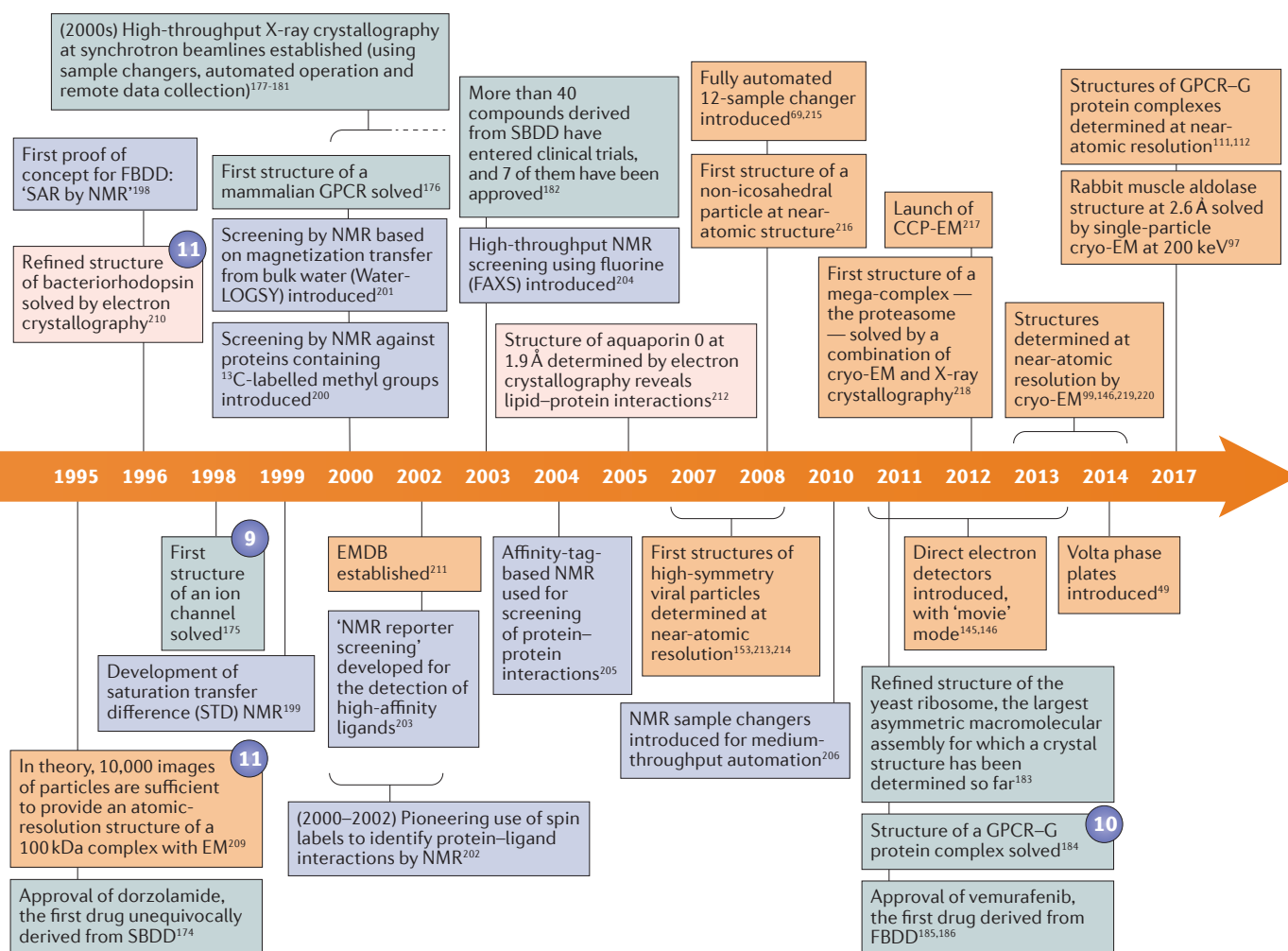
More recently, single-particle cryo-EM analysis has provided access to a rapidly growing number of high-resolution structures for objects not amenable to crystallization, including large, dynamic assemblies and membrane proteins, and technical advances have enabled the study of smaller objects and objects at higher resolution, including complexes with small molecules (TABLE 1). A selection of cryo-EM structures with drug discovery relevance is highlighted in this section, including membrane proteins (discussed in more depth in BOX 5).

### Membrane proteins

Among the membrane proteins for which cryo-EM structures have been solved,  $\gamma$ -secretase is a four-component 170 kDa intramembrane protease involved

in the cleavage of the amyloid- $\beta$  peptide. Dysfunction of  $\gamma$ -secretase is ultimately responsible for promoting amyloid plaque formation in the brains of individuals with early-onset Alzheimer disease, and for this reason it has attracted interest as a potential drug target.  $\gamma$ -Secretase is also involved in cancer as a key mediator of Notch signalling. The cryo-EM structure of  $\gamma$ -secretase solved at 3.4 Å resolution<sup>98</sup> revealed that the mutations causing early-onset Alzheimer disease map to two hot spots at the inner core of a four-transmembrane bundle, impairing protease activity. This atomic model could help to design more selective compounds against this challenging target. It is noteworthy that  $\gamma$ -secretase glycosylation had little effect on the structure reconstruction from cryo-EM data sets, whereas it could hamper crystallization for X-ray analysis.





Various ion channel structures have been solved at different resolutions, including several that are potential drug targets. These include the transient receptor potential cation channel subfamily V member 1 (TRPV1)<sup>99–101</sup> and TRPA1 (REF.<sup>102</sup>) channels, which are involved in sensing and transducing temperature and irritants, respectively; the voltage-gated calcium channel  $\text{Ca}_v1.1$  (REF.<sup>103</sup>) and sodium channel  $\text{Na}_v\text{PaS}$ <sup>104</sup>, which are involved in contraction of skeletal muscle tissue and in the generation and propagation of action potentials in excitable cells, respectively; and the glycine receptor, which mediates inhibitory synaptic transmission<sup>105</sup>. In particular, cryo-EM has had the greatest impact recently on studies of the channels in the TRP family, for which ~50 cryo-EM structures have been deposited in the past 4 years. Historically, obtaining well-diffracting crystals of TRP channels has been extremely difficult owing to their low levels of gene expression in cells and the conformational variability in response to chemical and physical stimuli. The structures of agonist-bound TRPV1 in nanodiscs (2.9 Å)<sup>101</sup>, TRPML3 (2.9 Å)<sup>106</sup> and TRPM4 in nanodiscs (2.9 Å)<sup>107</sup> are among the highest-resolution structures determined by single-particle cryo-EM for membrane proteins. Cryo-EM has also been invaluable in the study of extremely large ion channel complexes,

such as the Piezo-type mechanosensitive ion channel component 1 (PIEZO1)<sup>108</sup>, which is a widely produced 900 kDa mechanosensitive cation channel that has been linked to several human diseases, and the ryanodine receptors (RyRs)<sup>109,110</sup>, which are the largest known ion channels, with a mass of 2.2 MDa. They mediate intracellular  $\text{Ca}^{2+}$  release and are emerging therapeutic targets for heart diseases.

G protein-coupled receptors (GPCRs) are the most abundant cell-surface receptor proteins and are targeted by ~30% of drugs on the market. Although major progress has been made in recent years with X-ray crystallography of GPCRs (which had historically been very challenging), some members of this family are particularly refractory to study by this technique because of the challenges associated with obtaining high-quality crystals and their low stability in purified form. In addition, cryo-EM can enable the determination of the structures of subdomains in different conformations and GPCRs in complexes with their G protein partners, potentially clarifying relevant conformations to target with computational ligand screening. Improvements in the performance of cryo-EM have enabled GPCR researchers to image larger complexes that could not be crystallized because their conformational stability is too low. In 2016,

**Box 3 | X-ray crystallography compared with cryo-EM in drug discovery**

The key advantage of X-ray crystallography for drug discovery applications compared with cryo-electron microscopy (cryo-EM) is its ability to rapidly provide high-resolution structural data. Once a suitable crystallization system has been established, it takes very little time to obtain subsequent structures or screen compounds in rapid succession by X-ray crystallography. Around 2,000 crystallization conditions can be set up in 1 hour, with a further 2–3 hours needed to evaluate all the images to identify suitable crystallization conditions (which can be reduced with image recognition software). When screening to identify suitable samples and cryo-cooling conditions for EM, however, it is possible to evaluate only 12 samples in 1 session, with 3–4 hours needed to fully characterize them, which is orders of magnitude slower. Collecting a full X-ray data set at a synchrotron then takes less than 2 minutes; the subsequent data integration, structure solution and refinement of protein–ligand complexes has been automated to a large extent and is often completed within an hour.

Importantly, this means that the throughput of X-ray crystallography is sufficiently fast for ligand-screening campaigns in drug discovery. At present, data for ~500 crystals soaked with different compound fragments can be collected in 24 hours (for example, within the XChem framework at the Diamond synchrotron in the United Kingdom; see Related links), and the data can be processed online and refined within 1 week. To achieve the same thing with EM would require about half a year of data collection (assuming 8 hours per data set) and at least a year of computation and model building. Even with these optimistic timescale assumptions, ligand-screening campaigns would be 2–3 orders of magnitude slower using cryo-EM than using X-ray crystallography.

As noted in the main text, a key advantage of cryo-EM is that it can be readily used to determine the structure of large and/or dynamic macromolecules (including membrane proteins) in their native state, including post-translational modifications. Cryo-EM also typically requires much smaller amounts of protein than X-ray crystallography, which can be a particular advantage for demanding proteins. Indeed, for the use of X-ray crystallography in drug discovery, obtaining suitable crystals remains a key challenge that has a risk of delaying projects, especially for membrane proteins, heavily glycosylated proteins and large or flexible proteins or protein complexes. To address these challenges, a number of approaches have been developed, such as reducing large therapeutic targets to single domains in the hope of facilitating protein production, purification and crystallization while still capturing binding modes of potential drug candidates. This investment of time and resources at the beginning of a structured-guided drug discovery project is often mandatory to ensure sufficient throughput when screening hundreds of compounds.

Another important advantage of cryo-EM is that the phase information is directly and experimentally accessible in the reconstructed structures, whereas the phase information is lost in X-ray crystallography and has to be reconstructed by experimental phasing, which depends on the accuracy of experimental data collection. Consequently, especially for resolution levels in the range of 4–7.5 Å, structures determined by cryo-EM enable the visualization of individual domains and secondary structure elements with a clarity that is often not accessible by X-ray crystallography. However, the situation is different at resolution levels beyond 3 Å. Only a small fraction of the published cryo-EM structures have been reported at resolutions better than 3 Å, and in many cases the 3D maps cannot compete in quality with maps obtained by X-ray crystallography at comparable nominal resolutions. In this regard, it should be noted that resolution claims in X-ray crystallography and cryo-EM are based on very different measures and are therefore not directly comparable (see BOX 4).

Volta phase plate technology and cryo-EM single-particle analysis were used to determine the first cryo-EM structure (4.1 Å) of an activated GPCR, the human calcitonin receptor (a class B GPCR) in complex with salmon calcitonin and a G protein heterotrimer<sup>111</sup>. Soon after this initial success, the cryo-EM structure at 4.1 Å of the rabbit glucagon-like peptide 1 (GLP1) receptor bound to its activating peptide GLP1 and a G protein heterotrimer was solved, illustrating how a class B receptor is activated through hormone binding<sup>112</sup>, as well as the cryo-EM structure at 3.3 Å of the human GLP1 receptor bound to a G protein-biased agonist and a G protein heterotrimer, giving insight into biased agonism<sup>113</sup>. With a molecular mass of 150 kDa, this important drug target was considered practically impossible to image at near-atomic resolution using cryo-EM until recently. These GLP1 receptor structures, with the side chains clearly identifiable, could help to design new drugs for the treatment of type 2 diabetes and obesity. In addition, the structure of the human adenosine A<sub>2A</sub> receptor bound to an agonist and an engineered G protein heterotrimer was recently solved by cryo-EM at 4.5 Å resolution<sup>114</sup>; comparison with the structure of the same complex previously solved

by X-ray crystallography at 3.4 Å resolution<sup>115</sup> revealed flexible regions — in particular, and unexpectedly, in the ligand-binding pocket.

Cryo-EM has also revealed the structure of other membrane protein complexes refractory to X-ray diffraction structural analysis; for instance, to elucidate the mechanism of recognition of substrates by a eukaryotic ATP-binding cassette (ABC) transporter multidrug resistance-associated protein 1 (MRP1) and how the substrate binding stimulates ATP hydrolysis<sup>116</sup>. ABC transporters play a crucial role in the absorption, distribution, metabolism and elimination (ADME) of multiple drugs, potentially causing drug–drug interactions; therefore, information on their structures could be valuable in drug development.

**Other proteins**

Beyond membrane proteins, one recent key success of cryo-EM in gaining a structural understanding of a neurodegenerative disease target was the determination of the first high-resolution structures (3.4–3.5 Å) of tau filaments isolated from the brain of a patient with Alzheimer disease<sup>117</sup>, which is characterized by the



## Box 4 | Resolution claims in X-ray crystallography and cryo-EM

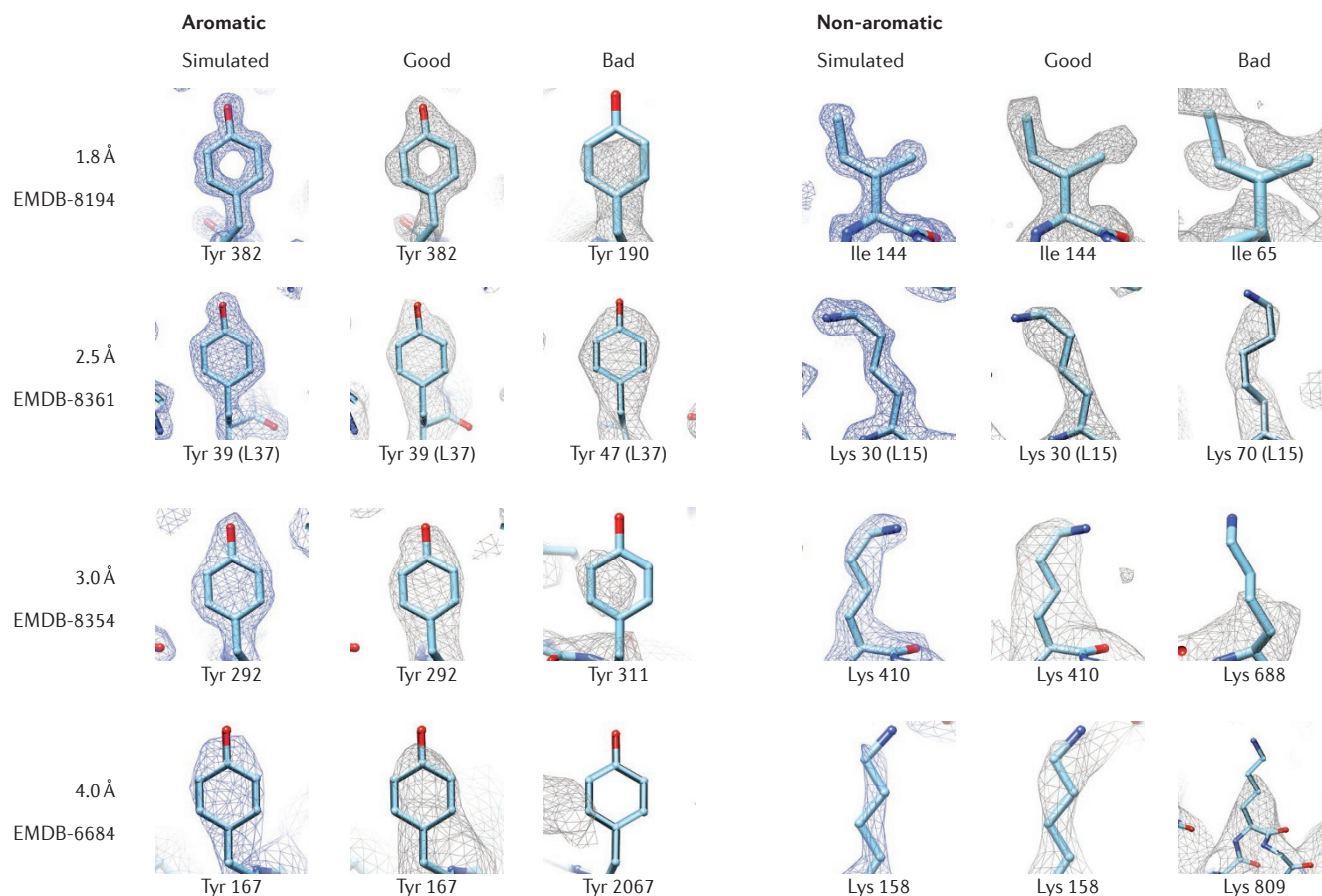
In X-ray crystallography, there is a direct measure of resolution based on the maximum diffraction of photons by the crystal lattice and other criteria that are based on statistics and the map versus atomic model comparison<sup>140</sup>. In cryo-electron microscopy (cryo-EM), the Fourier shell correlation (FSC) is generally used as the main resolution-determining tool, measuring the agreement of two independently determined 3D maps using half of the total data each<sup>141</sup>. The resolution is determined by the spatial frequency at which the correlation drops below a certain threshold value (mostly 0.143). The FSC represents a self-consistency measurement of the data processing; therefore, observed structural features in cryo-EM maps may sometimes deviate from expectations of how they are supposed to look at the claimed resolution. This is illustrated in the figure, which contains a selection of cryo-EM maps showing aromatic and non-aromatic residues visualized at different simulated and actually calculated resolutions. For the calculated resolution at each level, one well-visualized residue and one badly visualized residue are arbitrarily selected from the same model subjectively, without local resolution calculation being taken into consideration. At higher resolutions, the visualized feature differences between the simulated map (generated with UCSF Chimera) and the calculated map appear to be larger.

The FSC is also a global measure and thus provides only one average resolution value, which is misleading considering the amount of structural flexibility of macromolecules and the non-isotropic resolution distribution in typical cryo-EM maps. In the best-defined map regions, the resolution might be underestimated, whereas there are structural features in all cryo-EM maps that have much lower resolution than indicated by the FSC. It is also noteworthy that the FSC provides no information about the given quality of a calculated 3D map.

At present, there are numerous deposited cryo-EM 3D maps reporting resolutions around ~3.5 Å that appear to have better-defined structural

features (in their structurally well-defined areas) than X-ray crystallographic structures at 3.5 Å resolution. This is partially because the global resolution estimation of the FSC underestimates the resolution of the well-defined features, as noted above. However, it is also because X-ray-crystallography-based structure determination is technically difficult at resolutions >3.5 Å. The reason for that is that the observation-to-parameter ratio is poor in X-ray crystallography. Consequently, phase reconstruction from the collected amplitude data is inefficient, which is reflected in poor map quality at these resolutions. This situation is reversed at higher resolutions, when crystallographic data processing becomes increasingly more automated and reliable. By contrast, higher-resolution structure determination (<3 Å resolution) is much more difficult in cryo-EM compared to structures in the 3.5–4 Å resolution range. There are several parameters in cryo-EM structure determination that may contribute to this effect. For instance, it is very difficult to distinguish particle images that may belong to different conformations of a given macromolecular complex — a problem that becomes increasingly prominent with the number of different states present in one sample. Other effects such as beam damage and electron optical aberrations will also become increasingly limiting for high-resolution structure determination (<2.5 Å). Axial coma in particular will be the main resolution-limiting aberration in cryo-EM when aiming for reliable structure determination at <2 Å resolution.

A recently published study describes a multicriteria validation process designed to assess the agreement between a cryo-EM map and the corresponding atomic model that was applied to a set of 565 cryo-EM structures. The results indicate that reported resolutions may be overestimated in terms of expected structural features and that the highest resolution reached up to now using cryo-EM would apparently be 2.58 Å (EMD-2984)<sup>142</sup>.



## Box 5 | Cryo-EM studies of membrane proteins

Integral membrane proteins (IMPs) constitute ~30% of the proteome and represent the majority of the pharmaceutical target landscape<sup>130</sup>. They play fundamental roles in cells, including receptor signalling and transport of key molecules within the cell. Despite their importance, membrane proteins are structurally under-represented, reaching only ~3% of crystal structures in the Protein Data Bank (PDB) and only ~10% of entries in the Electron Microscopy Data Bank (EMDB). These numbers reflect the difficulty in obtaining a sufficient amount of stable and monodisperse membrane protein targets for structural characterization. In fact, overproduction, solubilization and stabilization of membrane proteins can each represent major hurdles that need to be overcome before initiating structural analysis. Historically, membrane protein structure determination has been carried out using X-ray crystallography or cryo-electron microscopy (cryo-EM) electron diffraction of 2D crystals. Both techniques require large amounts of purified protein and well-diffracting crystals. Although these techniques have yielded several high-resolution structures, many membrane protein targets have proved to be intractable to crystallization and therefore their structure determination requires alternative approaches.

In recent years, an increasing number of atomic or near-atomic resolution cryo-EM structures of IMPs have been determined, demonstrating the importance for cryo-EM in membrane protein drug discovery. Single-particle cryo-EM is particularly suitable for IMP structure determination because it overcomes the requirement of large amounts of protein and the need for obtaining diffracting crystals. Nevertheless, some additional biochemical steps need to be taken in order to employ cryo-EM for membrane protein samples. IMPs are generally solubilized in detergents at concentrations higher than the critical micellar concentration (CMC) for purification. At these concentrations, the free detergent can severely influence ice thickness and image contrast and, having a comparable intensity of the protein particles in examination, can therefore affect particle picking and data processing. For this reason, several approaches have been explored to reduce or replace detergent during cryo-EM grid preparation for IMPs. An effective method to reduce the detergent concentration is GraDeR (gradient-based detergent removal), which combines the strengths of GraFix<sup>55</sup> with simultaneous detergent removal<sup>131</sup>. More widely used are methods that exchange detergents with amphipols<sup>132</sup>, nanodiscs<sup>133</sup> and engineered  $\beta$ -sheet peptides<sup>134</sup>.

Similar to other protein complexes, membrane proteins can adopt multiple conformations in solution. This heterogeneity can be represented either by a continuous motion or by a series of discrete states. One advantage of cryo-EM over X-ray crystallography is the ability to computationally sort this structural heterogeneity into distinct classes using maximum likelihood methods<sup>135,136</sup>. When the system adopts a series of discrete states, it is possible to isolate and determine multiple higher-resolution structures, each for a specific conformational state. In the case of the F-ATPase, it was possible to isolate seven distinct states from a single data set, which provides insights into the catalytic activity of these motors<sup>137</sup>.

With the introduction of direct electron detectors, cryo-EM has now been used to visualize a large number of membrane proteins and obtain medium-resolution to high-resolution structures. Some of the recent membrane protein structures determined by single-particle cryo-EM include enzymes such as  $\gamma$ -secretase<sup>98</sup>, ion channels such as transient receptor potential cation channel subfamily V member 1 (TRPV1)<sup>101</sup> and TRPA1 (REF. <sup>102</sup>), voltage-gated calcium channel  $\text{Ca}_v1.1$  (REF. <sup>103</sup>) and sodium channel  $\text{Na}_v\text{PaS}^{104}$ , membrane protein complexes such as a class B G protein-coupled receptor (GPCR)-G protein complex<sup>111</sup> and transporters such as multidrug resistance-associated protein 1 (MRP1)<sup>116</sup>, ATP-binding cassette subfamily G member 2 (ABCG2)<sup>138</sup> and tip-associated protein (TAP; also known as NXF1)<sup>139</sup>, with sizes spanning between ~100 kDa and >2 MDa (see main text for discussion of specific examples).

Although single-particle cryo-EM has proved to be successful for membrane protein structure determination, a few additional advancements in the field promise to increase the success of this technology applied to membrane proteins and drug discovery. Improvements to microscopes, detectors and computational methods as well as addition of monoclonal antigen-binding fragments (Fabs) and new advances in phase plate technology will allow high-resolution structure determination of smaller protein complexes (<100 kDa). The further development of 'on-grid purification technology' (REF. <sup>60</sup>) could allow the capture of membrane proteins directly on the EM grid. This technology could provide structural insights for systems in which protein levels are very low or overproduction of the target is not possible. In addition, although cryo-EM and single-particle analysis can provide atomic structure of purified samples, we recommend studying these complexes in their native environment because membrane potential and environment affect the mechanism of function of these complexes. With the direct electron detectors and cryo-EM subtomogram averaging, it is now possible to obtain subnanometre structures of macromolecules in their native environment. Further advances will probably move these characterizations towards atomic resolution in the next few years.

In summary, cryo-EM is rapidly becoming the technique of choice for membrane protein structure determination. Additional biochemical, technological and computational developments will allow atomic structure determination for small asymmetric membrane protein complexes, in a variety of conformational states, potentially in their native environment.

presence of neurofibrillary tau aggregates that are composed of paired helical filaments (PHFs) and straight filaments (SFs). The cryo-EM structures of PHFs and SFs shed light on the differences between molecular conformers of tau aggregates, indicating how different isoforms are incorporated into the filaments. Enabling high-resolution structure determination of these filaments opens up new possibilities for structure-based

drug discovery, such as the design of specific aggregation inhibitors. Along the same lines, the cryo-EM structure of amyloid- $\beta$ (1–42) fibrils at 4.0 Å should provide insights into the mechanism of amyloid plaque formation<sup>118</sup>.

It is also worth mentioning the recently reported cryo-EM structures of microtubules in complex with various anticancer compounds acting as stabilizers, elucidating distinct mechanisms<sup>119</sup>.

### Antibodies and vaccines

An important issue in understanding the mechanisms of action of potential biotherapeutics is the elucidation of monoclonal antibody (mAb) activity by epitope mapping analysis. In recent years, negative staining and cryo-EM have been used for both linear and conformational epitope mapping. This method requires only microgram amounts of the antibody–antigen complex and can be used in combination with other epitope mapping technologies, such as hydrogen–deuterium exchange mass spectrometry (HDX-MS) or fast photochemical oxidation of proteins (FPOP), to determine epitopes at the amino acid level. Among recent examples, Long and colleagues used cryo-EM to elucidate how two highly protective chikungunya-virus-neutralizing human mAbs bind to virus-like particles and block the fusion of viral and host membranes<sup>120</sup>. Classic transmission EM (TEM) using negative staining can provide useful information leading scientists to a promising path or at least to avoid dead ends. Ciferri and colleagues used negative-staining microscopy to investigate the structure of an antibody that forms a distinct complex with HTRA1, a serine protease implicated in age-related macular degeneration, and inhibits its enzymatic activity<sup>121</sup>. The study highlighted the cage-like structure of the immunoglobulin G (IgG)–HTRA1 complex having a higher potency than its Fab counterpart by forming a less compact propeller-like arrangement and identified the antibody binding site and the associated inhibition mechanism<sup>121</sup>. Using new cryo-TEM technologies could further enable epitope mapping to support rational mAb design.

The HIV-1 envelope glycoprotein gp160 trimer (Env) allows the virus to attach to CD4<sup>+</sup> helper T cells, fuse its viral envelope and initiate the infectious cycle. As a major target for broadly neutralizing antibodies (bnAbs), the Env structure is a central focus for HIV vaccine design. Lee and colleagues compared the cryo-EM structure of the native Env (just missing its cytoplasmic tail) stabilized by the bnAbs PGT151 and 10E8 with soluble Env trimers being developed as vaccine candidates<sup>122</sup>. Their results show that native Env has its hydrophobic membrane proximal external region (MPER) shielded in the unliganded state, whereas it undergoes a large conformational rearrangement when it is bound to the MPER-targeting antibody 10E8. The results show that Env is a difficult, dynamic target for the immune system. Also of value for vaccine design, the initial quaternary interaction between the CD4 receptor and the HIV-1 Env trimer has recently been elucidated by cryo-EM<sup>123</sup>.

### Potential in hit-to-lead and lead optimization

A question that is currently of great interest to drug discovery researchers is whether or not cryo-EM can yet be used for the hit-to-lead and lead-optimization stages, which often rely on SBDD when the target 3D structure is available. For SBDD to be useful at these stages, a fast and robust pipeline to produce multiple structures in a short time frame (compared with the drug candidate development time) is a prerequisite, and

high-throughput X-ray crystallography has long been the gold-standard technique when the target can be crystallized. Co-crystallization or crystal soaking with series of compounds are used to generate co-crystals that feed a pipeline, including X-ray diffraction data collection at a synchrotron source, molecular replacement and ligand building in a high-throughput, automated fashion, yielding multiple structures of compound–target complexes. Resolution should ideally be better than ~2.5 Å for structural information to be effectively exploited for drug design.

Although recent progress in cryo-EM has allowed structures of compound–target complexes to be determined at resolutions below 3 Å (TABLE 1), suggesting an upcoming important role for cryo-EM in SBDD, its full applicability is far from being routine at present. For example, one limitation is the time frame involved in obtaining high-resolution cryo-EM structures, which are not yet compatible with those of drug discovery campaigns and are still slower than X-ray crystallography by a few orders of magnitude (BOX 3). Nevertheless, a few examples illustrate the potential of cryo-EM if the limitations can be addressed. Merk and colleagues determined the cryo-EM structure at 3.8 Å resolution of isocitrate dehydrogenase (93 kDa) and structurally characterized the conformational changes induced by the binding of a small-molecule inhibitor<sup>25</sup>. Wong and colleagues determined the cryo-EM structures of the *Plasmodium falciparum* 80S ribosome bound to the anti-protozoan drugs emetine at 3.2 Å (REF. <sup>124</sup>) and mefloquine at 3.2 Å (REF. <sup>125</sup>), representing the first examples of compounds binding to a ribosome for which the binding site was previously unknown.

Although the use of cryo-EM in the design of new lead compounds has not yet been reported, these promising results and ongoing technological improvements in the steps of the cryo-EM process discussed in the previous section suggest that cryo-EM will soon be considered one key tool for SBDD, particularly for targets that are difficult to crystallize, such as membrane proteins. As the rate of near-atomic-resolution structures produced by cryo-EM increases, interest and expectations from the pharmaceutical industry are growing.

### Outlook for cryo-EM in drug discovery

In just a few years, exciting advances in cryo-EM have propelled this technology from the era of ‘blob-ology’ — infamous for delivering results with a lot of room for interpretation — into an era in which it is possible to obtain near-atomic resolution structures of biomolecules without the time-consuming and often difficult hunt for suitable crystals for X-ray analysis. Today, structural biologists are using cryo-EM to investigate the structure and function of large protein complexes, large cellular machines and viruses at near-atomic resolution. A number of case studies, such as those discussed above, have shown that it is now possible to use the method on well-behaved systems to clearly depict density for amino acid side chains, for small, drug-like molecules that are tightly bound to proteins and in some cases even to determine the position of water molecules. The minimal

particle size barrier has gradually been lowered<sup>24,126</sup>, and such technology combined with improved sample grid preparation will probably soon result in more structures of small membrane proteins. These advances are fuelling hopes that future developments will soon ring in the dawn of a “golden age where resolutions of 2 Å can be routinely achieved” (REF. 127) and are even raising the expectation that cryo-EM will be quick and efficient enough to compete with, or even replace, crystallography for many applications<sup>128</sup>.

Indeed, for some applications in the pharmaceutical industry, cryo-EM already has substantial appeal, as it might not always be necessary to achieve resolutions below 4 Å to address various questions that are raised at the very start of a drug discovery process. Lower-resolution structures may be of great benefit for a better understanding of the target biology and the identification of binding pockets that are located between domains or binding partners of a protein complex — pockets that are not even present when looking just at an isolated domain. It also may not always be necessary to exactly determine the binding mode of a compound; for example, showing a distinct effect of ligand binding that leads to the induction of conformational changes may also speed up the drug discovery process or even expand the available target space. In addition, although the resolution of a structural analysis by cryo-EM is often limited by the wide range of conformation states in a data set, this limitation can be turned into an advantage for SBDD as reconstruction of various intermediate states could help to understand the dynamics of a system and explain how a complex binds to its substrate.

To make use of these opportunities, multiple companies have already increased their focus on cryo-EM, using a variety of approaches to collect and process EM data. These include partnering with academic laboratories (through collaborations or fee-for-service), use of external contract research organizations (CROs) or centralized facilities and establishment of consortia with additional partners or in-house facilities. Establishing a collaborative and/or fee-for-service agreement with academic laboratories that have set up state-of-the-art facilities may be the least expensive and easiest approach for companies. Generally, with a very reasonable budget, it is possible to collect a sufficient amount of data to support individual projects without facing the high costs of purchasing or maintaining the instrumentation and without the need for in-house cryo-EM expertise. A comparable scenario is represented by the use of CROs, where the higher associated cost (often prohibitive for smaller companies) than the cost of collaborating with academia is typically associated with better instrumentation and support available. However, although these two models are effective, especially if used while planning for capital investment or establishing in-house facilities, they are not sufficient when several data sets per year are required. In this respect, the synchrotron-like facilities that have emerged in the past few years with the promise to facilitate usage of cryo-EM may enable what has been described as the ‘democratization of cryo-EM’ (REF. 129). Among these, iNEXT (a

consortium of several cryo-EM institutions including Diamond, EMBL and NeCEN), the Janelia Farm campus of the Howard Hughes Medical Institute and the US National Cancer Institute are enabling users to access high-end cryo-EM infrastructures. However, although these centres offer state-of-the-art technology and outstanding support, they are almost entirely devoted to supporting academic institutions and are often highly oversubscribed, leaving little to no space to support cryo-EM in industry.

Although the upcoming synchrotron-like facilities promise to support the growing need for cryo-EM, there are limitations. In crystallography, a full data set on a crystal can be collected in just a few minutes and structures can be generated very rapidly, making it a great resource for small-molecule projects in which several structures are needed (BOX 3). In cryo-EM, each data collection spans the course of several hours or days, making the throughput for cryo-EM much slower than crystallography. In addition, cryo-EM sample preparation often requires a great deal of optimization, requiring the ability to screen several samples before being in the position to collect a high-resolution data set. This is not possible with the current limited access to these facilities.

To overcome these limitations, several cryo-EM groups in industry have established consortia, by partnering with other industrial institutions, to establish state-of-the-art facilities in which each member can make use of a fraction of the available time. These consortia often include an academic institution with the scope of providing expertise and know-how to support data collection and processing. The Cambridge Pharmaceutical cryo-EM Consortium in the United Kingdom is an example of this model. Here, Thermo Fisher Scientific, together with five pharmaceutical companies (Astex Pharmaceuticals, AstraZeneca, GlaxoSmithKline, Heptares Therapeutics and UCB), share access to the Titan Krios microscope with colleagues from the MRC Laboratory of Molecular Biology and the University of Cambridge. Some companies have made an even greater commitment to cryo-EM by establishing state-of-the-art in-house facilities. Among these, Pfizer, Novartis and Genentech hired several experts in the field and invested in high-end microscopes and in computational infrastructures with the goal of collecting several data sets a year to support large-molecule and small-molecule research programmes.

Apart from the race for ever more powerful (and, in general, more expensive) microscopes, optimization of the use of existing machines can also be quite effective. For instance, a rabbit muscle aldolase structure at 2.6 Å resolution was recently obtained using a 200 keV, lower-range microscope optimized for single-particle analysis<sup>97</sup>, demonstrating the possible access to fairly high resolutions at a reduced cost of ownership.

Although it is hard to predict which model for generating cryo-EM data will be the most successful, cryo-EM use in industry is rapidly increasing and will continue to do so in the next several years. Nevertheless, for routine drug discovery, a number of tools still need to be



developed before cryo-EM can become the method of choice for drug hunters. It certainly requires the introduction of robust workflows, and the development of cost-effective and more reliable equipment will also help to encourage the use of cryo-EM. It will be necessary to increase the throughput of data collection before the method can compete with crystallography or NMR during the screening process or during hit validation, and the potential for the use of cryo-EM during compound optimization would be substantially greater if the time from grid preparation to the finished structure can be reduced. Developing clearly defined criteria that help modellers, chemists and biologists to assess the quality of an EM map or structure will be necessary.

Finally, the use of cryo-EM in drug discovery will not only hinge on the developments in the cryo-EM field but may also depend on further advances in crystallography. When looking today at the well-established, largely automated workflows that produce crystal structures with easily quantifiable quality criteria at an increasingly fast pace, it is difficult to imagine how cryo-EM might replace crystallography for routine drug discovery in the next few years. It seems more likely that the two technologies will remain as complementary approaches for drug discovery for some time, although the boundaries that determine the method of choice have begun shifting in favour of cryo-EM and will continue to do so.

1. von Borries, B. E. & Ruska, H. R. Bakterien und Virus in übermikroskopischer Aufnahme. *J. Mol. Med.* **17**, 921–925 (1938).
2. Kausche, G. A., Pfankuch, E. & Ruska, H. Die Sichtbarmachung von pflanzlichem Virus im Übermikroskop. *Naturwissenschaften* **27**, 292–299 (1939).
3. Kruger, D. H., Schneck, P. & Gelderblom, H. R. Helmut Ruska and the visualisation of viruses. *Lancet* **355**, 1713–1717 (2000).
4. Dubochet, J. & McDowell, A. W. Vitrification of pure water for electron microscopy. *J. Microsc.* **124**, RP3–RP4 (1981).
5. Dubochet, J., Lepault, J., Freeman, R., Berriman, J. A. & Homo, J.-C. Electron microscopy of frozen water and aqueous solutions. *J. Microsc.* **128**, 219–237 (1982).
6. Dubochet, J., Chang, J.-J., Freeman, R., Lepault, J. & McDowell, A. W. Frozen aqueous suspensions. *Ultramicroscopy* **10**, 55–62 (1982).
7. Adrian, M., Dubochet, J., Lepault, J. & McDowell, A. W. Cryo-electron microscopy of viruses. *Nature* **308**, 32–36 (1984).
8. van Heel, M. & Frank, J. Use of multivariate statistics in analysing the images of biological macromolecules. *Ultramicroscopy* **6**, 187–194 (1981).
9. Frank, J., Shimkin, B. & Dowse, H. Spider—a modular software system for electron image processing. *Ultramicroscopy* **6**, 343–357 (1981).
10. van Heel, M. & Keegstra, W. IMAGIC: a fast, flexible and friendly image analysis software system. *Ultramicroscopy* **7**, 113–129 (1981).
11. Penczek, P., Radermacher, M. & Frank, J. Three-dimensional reconstruction of single particles embedded in ice. *Ultramicroscopy* **40**, 33–53 (1992).
12. Frank, J. et al. SPIDER and WEB: processing and visualization of images in 3D electron microscopy and related fields. *J. Struct. Biol.* **116**, 190–199 (1996).
13. Marabini, R. et al. Xmipp: an image processing package for electron microscopy. *J. Struct. Biol.* **116**, 237–240 (1996).
14. Suloway, C. et al. Automated molecular microscopy: the new Legion system. *J. Struct. Biol.* **151**, 41–60 (2005).
15. Mastronarde, D. N. Automated electron microscope tomography using robust prediction of specimen movements. *J. Struct. Biol.* **152**, 36–51 (2005).
16. Lander, G. C. et al. Appion: an integrated, database-driven pipeline to facilitate EM image processing. *J. Struct. Biol.* **166**, 95–102 (2009).
17. van Heel, M. et al. in *International Tables for Crystallography, Volume F, 2nd Edition, Crystallography of Biological Macromolecules* (eds Arnold, E., Himmel, D. M. & Rossmann, M. G.) 624–628 (Wiley, 2012).
18. Kimanius, D., Forsberg, B. O., Scheres, S. H. & Lindahl, E. Accelerated cryo-EM structure determination with parallelisation using GPUs in RELION-2. *eLife* **5**, e18722 (2016).
19. Bell, J. M., Chen, M., Baldwin, P. R. & Ludtke, S. J. High resolution single particle refinement in EMAN2.1. *Methods* **100**, 25–34 (2016).
20. Punjani, A., Rubinstein, J. L., Fleet, D. J. & Brubaker, M. A. cryoSPARC: algorithms for rapid unsupervised cryo-EM structure determination. *Nat. Methods* **14**, 290–296 (2017).
21. Grant, T. Rohou, A. & Grigorieff, N. cisTEM, user-friendly software for single-particle image processing. *eLife* **7**, e35383 (2018).
22. Kuhlbrandt, W. Biochemistry. The resolution revolution. *Science* **343**, 1443–1444 (2014).
23. Bai, X. C., McMullan, G. & Scheres, S. H. How cryo-EM is revolutionizing structural biology. *Trends Biochem. Sci.* **40**, 49–57 (2015).
24. Khoshouei, M., Radjainia, M., Baumeister, W. & Danev, R. Cryo-EM structure of haemoglobin at 3.2 Å determined with the Volta phase plate. *Nat. Commun.* **8**, 16099 (2017).
25. Merk, A. et al. Breaking cryo-EM resolution barriers to facilitate drug discovery. *Cell* **165**, 1698–1707 (2016).
26. Blundell, T. L. & Patel, S. High-throughput X-ray crystallography for drug discovery. *Curr. Opin. Pharmacol.* **4**, 490–496 (2004).
27. Blundell, T. L. et al. Structural biology and bioinformatics in drug design: opportunities and challenges for target identification and lead discovery. *Phil. Trans. R. Soc. B* **361**, 413–423 (2006).
28. Pellecchia, M. et al. Perspectives on NMR in drug discovery: a technique comes of age. *Nat. Rev. Drug Discov.* **7**, 738–745 (2008).
29. Zheng, H. et al. X-Ray crystallography over the past decade for novel drug discovery - where are we heading next? *Expert Opin. Drug Discov.* **10**, 975–989 (2015).
30. Campbell, M. G. et al. Movies of ice-embedded particles enhance resolution in electron cryo-microscopy. *Structure* **20**, 1823–1828 (2012).
31. Grant, T. & Grigorieff, N. Automatic estimation and correction of anisotropic magnification distortion in electron microscopes. *J. Struct. Biol.* **192**, 204–208 (2015).
32. Briot, A. F. et al. Beam-induced motion of vitrified specimen on holey carbon film. *J. Struct. Biol.* **177**, 630–637 (2012).
33. Zheng, S. Q. et al. MotionCor2: anisotropic correction of beam-induced motion for improved cryo-electron microscopy. *Nat. Methods* **14**, 331–332 (2017).
34. Russo, C. J. & Passmore, L. A. Electron microscopy: ultrastable gold substrates for electron cryomicroscopy. *Science* **346**, 1377–1380 (2014).
35. Russo, C. J. & Passmore, L. A. Robust evaluation of 3D electron cryomicroscopy data using tilt-pairs. *J. Struct. Biol.* **187**, 112–118 (2014).
36. Stark, H., Zemlin, F. & Boettcher, C. Electron radiation damage to protein crystals of bacteriorhodopsin at different temperatures. *Ultramicroscopy* **63**, 75–79 (1996).
37. Grant, T. & Grigorieff, N. Measuring the optimal exposure for single particle cryo-EM using a 2.6 Å reconstruction of rotavirus VP6. *eLife* **4**, e06980 (2015).
38. Radermacher, M., Wagenknecht, T., Verschoor, A. & Frank, J. Three-dimensional reconstruction from a single-exposure, random conical tilt series applied to the 50S ribosomal subunit of *Escherichia coli*. *J. Microsc.* **146**, 113–136 (1987).
39. Grigorieff, N. FREALIGN: high-resolution refinement of single particle structures. *J. Struct. Biol.* **157**, 117–125 (2007).
40. Reboul, C. F., Eager, M., Elmlund, D. & Elmlund, H. Single-particle cryo-EM-improved ab initio 3D reconstruction with SIMPLE/PRIME. *Protein Sci.* **27**, 51–61 (2018).
41. Scheres, S. H. RELION: implementation of a Bayesian approach to cryo-EM structure determination. *J. Struct. Biol.* **180**, 519–530 (2012).
42. Unverdorben, P. et al. Deep classification of a large cryo-EM dataset defines the conformational landscape of the 26S proteasome. *Proc. Natl Acad. Sci. USA* **111**, 5544–5549 (2014).
43. Bai, X. C., Rajendra, E., Yang, G., Shi, Y. & Scheres, S. H. Sampling the conformational space of the catalytic subunit of human gamma-secretase. *eLife* **4**, e11182 (2015).
44. von Loeffelholz, O. et al. Focused classification and refinement in high-resolution cryo-EM structural analysis of ribosome complexes. *Curr. Opin. Struct. Biol.* **46**, 140–148 (2017).
45. Tagare, H. D., Barthel, A. & Sigworth, F. J. An adaptive expectation-maximization algorithm with GPU implementation for electron cryomicroscopy. *J. Struct. Biol.* **171**, 256–265 (2010).
46. Glaeser, R. M. & Hall, R. J. Reaching the information limit in cryo-EM of biological macromolecules: experimental aspects. *Biophys. J.* **100**, 2331–2337 (2011).
47. Thompson, R. F., Walker, M., Siebert, C. A., Muench, S. P. & Ranson, N. A. An introduction to sample preparation and imaging by cryo-electron microscopy for structural biology. *Methods* **100**, 3–15 (2016).
48. Zernike, F. How I discovered phase contrast. *Science* **121**, 345–349 (1955).
49. Danev, R., Buijsse, B., Khoshouei, M., Plitzko, J. M. & Baumeister, W. Volta potential phase plate for in-focus phase contrast transmission electron microscopy. *Proc. Natl Acad. Sci. USA* **111**, 15635–15640 (2014).
50. Danev, R., Tegunov, D. & Baumeister, W. Using the Volta phase plate with defocus for cryo-EM single particle analysis. *eLife* **6**, e23006 (2017).
51. Danev, R. & Baumeister, W. Expanding the boundaries of cryo-EM with phase plates. *Curr. Opin. Struct. Biol.* **46**, 87–94 (2017).
52. Wu, S. et al. Fabs enable single particle cryoEM studies of small proteins. *Structure* **20**, 582–592 (2012).
53. Liu, Y., Gonen, S., Gonen, T. & Yeates, T. O. Near-atomic cryo-EM imaging of a small protein displayed on a designed scaffolding system. *Proc. Natl Acad. Sci. USA* **115**, 3362–3367 (2018).
54. Chari, A. et al. ProteoPlex: stability optimization of macromolecular complexes by sparse-matrix screening of chemical space. *Nat. Methods* **12**, 859–865 (2015).
55. Kastner, B. et al. GraFix: sample preparation for single-particle electron cryomicroscopy. *Nat. Methods* **5**, 53–55 (2008).
56. Ericsson, U. B., Hallberg, B. M., Detitta, G. T., Dekker, N. & Nordlund, P. Thermofluor-based high-throughput stability optimization of proteins for structural studies. *Anal. Biochem.* **357**, 289–298 (2006).
57. Boivin, S., Kozak, S. & Meijers, R. Optimization of protein purification and characterization using thermofluor screens. *Protein Expr. Purif.* **91**, 192–206 (2013).
58. Benjamin, C. J. et al. Nonfouling NTA-PEG-based TEM grid coatings for selective capture of histidine-tagged protein targets from cell lysates. *Langmuir* **32**, 551–559 (2016).
59. Benjamin, C. J. et al. Selective capture of histidine-tagged proteins from cell lysates using TEM grids modified with NTA-graphene oxide. *Sci. Rep.* **6**, 32500 (2016).

60. Yu, G., Li, K. & Jiang, W. Antibody-based affinity cryo-EM grid. *Methods* **100**, 16–24 (2016).
61. Yu, G., Li, K., Huang, P., Jiang, X. & Jiang, W. Antibody-based affinity cryoelectron microscopy at 2.6-Å resolution. *Structure* **24**, 1984–1990 (2016).
62. Russo, C. J. & Passmore, L. A. Controlling protein adsorption on graphene for cryo-EM using low-energy hydrogen plasmas. *Nat. Methods* **11**, 649–652 (2014).
63. Sader, K., Stopps, M., Calder, L. J. & Rosenthal, P. B. Cryomicroscopy of radiation sensitive specimens on unmodified graphene sheets: reduction of electron-optical effects of charging. *J. Struct. Biol.* **183**, 531–536 (2013).
64. Pantelic, R. S., Meyer, J. C., Kaiser, U., Baumeister, W. & Plitzko, J. M. Graphene oxide: a substrate for optimizing preparations of frozen-hydrated samples. *J. Struct. Biol.* **170**, 152–156 (2010).
65. Snijder, J. et al. Vitrification after multiple rounds of sample application and blotting improves particle density on cryo-electron microscopy grids. *J. Struct. Biol.* **198**, 38–42 (2017).
66. Adrian, M., Dubochet, J., Fuller, S. D. & Harris, J. R. Cryo-negative staining. *Micron* **29**, 145–160 (1998).
67. Heymann, J. B., Cardone, G., Winkler, D. C. & Steven, A. C. Computational resources for cryo-electron tomography in Bsoft. *J. Struct. Biol.* **161**, 232–242 (2008).
68. Korinek, A., Beck, F., Baumeister, W., Nickell, S. & Plitzko, J. M. Computer controlled cryo-electron microscopy—TOM(2) a software package for high-throughput applications. *J. Struct. Biol.* **175**, 394–405 (2011).
69. Coudray, N. et al. Automated screening of 2D crystallization trials using transmission electron microscopy: a high-throughput tool-chain for sample preparation and microscopic analysis. *J. Struct. Biol.* **173**, 365–374 (2011).
70. Harris, J. R. & Adrian, M. Preparation of thin-film frozen-hydrated/vitrified biological specimens for cryoelectron microscopy. *Methods Mol. Biol.* **117**, 31–48 (1999).
71. Chen, B. et al. Structural dynamics of ribosome subunit association studied by mixing-spraying time-resolved cryogenic electron microscopy. *Structure* **23**, 1097–1105 (2015).
72. Razinkov, I. et al. A new method for vitrifying samples for cryoEM. *J. Struct. Biol.* **195**, 190–198 (2016).
73. Feng, X. et al. A fast and effective microfluidic spraying-plunging method for high-resolution single-particle cryo-EM. *Structure* **25**, 663–670 e663 (2017).
74. Berriman, J. & Unwin, N. Analysis of transient structures by cryo-microscopy combined with rapid mixing of spray droplets. *Ultramicroscopy* **56**, 241–252 (1994).
75. Lu, Z. et al. Monolithic microfluidic mixing-spraying devices for time-resolved cryo-electron microscopy. *J. Struct. Biol.* **168**, 388–395 (2009).
76. Shaikh, T. R. et al. Initial bridges between two ribosomal subunits are formed within 9.4 milliseconds, as studied by time-resolved cryo-EM. *Proc. Natl Acad. Sci. USA* **111**, 9822–9827 (2014).
77. Arnold, S. A. et al. Blotting-free and lossless cryo-electron microscopy grid preparation from nanoliter-sized protein samples and single-cell extracts. *J. Struct. Biol.* **197**, 220–226 (2017).
78. Langmore, J. P. & Smith, M. F. Quantitative energy-filtered electron microscopy of biological molecules in ice. *Ultramicroscopy* **46**, 349–373 (1992).
79. Orlova, E. V. & Saibil, H. R. Structural analysis of macromolecular assemblies by electron microscopy. *Chem. Rev.* **111**, 7710–7748 (2011).
80. Bartesaghi, A. et al. 2.2 Å resolution cryo-EM structure of beta-galactosidase in complex with a cell-permeant inhibitor. *Science* **348**, 1147–1151 (2015).
81. Glaeser, R. M. et al. Factors that influence the formation and stability of thin, cryo-EM specimens. *Biophys. J.* **110**, 749–755 (2016).
82. Glaeser, R. M. & Han, B. G. Opinion: hazards faced by macromolecules when confined to thin aqueous films. *Biophys. Rep.* **3**, 1–7 (2017).
83. Russo, C. J. & Passmore, L. A. Progress towards an optimal specimen support for electron cryomicroscopy. *Curr. Opin. Struct. Biol.* **37**, 81–89 (2016).
84. Tan, Y. Z. et al. Addressing preferred specimen orientation in single-particle cryo-EM through tilting. *Nat. Methods* **14**, 793–796 (2017).
85. Trinick, J. & Cooper, J. Concentration of solutes during preparation of aqueous suspensions for cryo-electron microscopy. *J. Microsc.* **159**, 215–222 (1990).
86. Egelhaaf, S. U., Schurtenberger, P. & Muller, M. New controlled environment vitrification system for cryo-transmission electron microscopy: design and application to surfactant solutions. *J. Microsc.* **200**, 128–139 (2000).
87. Ge, H., Suszynski, W. J., Davis, H. T. & Scriven, L. E. New controlled environment vitrification system for preparing wet samples for cryo-SEM. *J. Microsc.* **229**, 115–126 (2008).
88. Iancu, C. V. et al. Electron cryotomography sample preparation using the Vitrobot. *Nat. Protoc.* **1**, 2813–2819 (2006).
89. Resch, G. P., Brandstetter, M., Konigsmaier, L., Urban, E. & Pickl-Herk, A. M. Immersion freezing of suspended particles and cells for cryo-electron microscopy. *Cold Spring Harb. Protoc.* **2011**, 803–814 (2011).
90. Kasas, S., Dumas, G., Dietler, G., Catsicas, S. & Adrian, M. Vitrification of cryoelectron microscopy specimens revealed by high-speed photographic imaging. *J. Microsc.* **211**, 48–53 (2003).
91. Noble, A. J. et al. Routine single particle CryoEM sample and grid characterization by tomography. *bioRxiv* <https://doi.org/10.1101/230276> (2017).
92. Wang, R. Y. et al. De novo protein structure determination from near-atomic-resolution cryo-EM maps. *Nat. Methods* **12**, 335–338 (2015).
93. Zhou, N., Wang, H. & Wang, J. EMBuild: a template matching-based automatic model-building program for high-resolution Cryo-electron microscopy maps. *Sci. Rep.* **7**, 2664 (2017).
94. Wang, R. Y. et al. Automated structure refinement of macromolecular assemblies from cryo-EM maps using Rosetta. *eLife* **5**, e17219 (2016).
95. Singhroy, A. et al. Molecular dynamics-based refinement and validation for sub-5 Å cryo-electron microscopy maps. *eLife* **5**, e16105 (2016).
96. Jakobi, A. J., Wilmanns, M. & Sachse, C. Model-based local density sharpening of cryo-EM maps. *eLife* **6**, e27131 (2017).
97. Herzik, M. A. Jr., Wu, M. & Lander, G. C. Achieving better-than-3-Å resolution by single-particle cryo-EM at 200 keV. *Nat. Methods* **14**, 1075–1078 (2017).
98. Bai, X. C. et al. An atomic structure of human gamma-secretase. *Nature* **525**, 212–217 (2015).
99. Liao, M., Cao, E., Julius, D. & Cheng, Y. Structure of the TRPV1 ion channel determined by electron cryo-microscopy. *Nature* **504**, 107–112 (2013).
100. Cao, E., Liao, M., Cheng, Y. & Julius, D. TRPV1 structures in distinct conformations reveal activation mechanisms. *Nature* **504**, 113–118 (2013).
101. Gao, Y., Cao, E., Julius, D. & Cheng, Y. TRPV1 structures in nanodiscs reveal mechanisms of ligand and lipid action. *Nature* **534**, 347–351 (2016).
102. Paulsen, C. E., Armache, J. P., Gao, Y., Cheng, Y. & Julius, D. Structure of the TRPA1 ion channel suggests regulatory mechanisms. *Nature* **520**, 511–517 (2015).
103. Wu, J. et al. Structure of the voltage-gated calcium channel Ca<sub>v</sub>1.1 at 3.6 Å resolution. *Nature* **537**, 191–196 (2016).
104. Shen, H. et al. Structure of a eukaryotic voltage-gated sodium channel at near-atomic resolution. *Science* **355**, eaal4326 (2017).
105. Du, J., Lu, W., Wu, S., Cheng, Y. & Gouaux, E. Glycine receptor mechanism elucidated by electron cryo-microscopy. *Nature* **526**, 224–229 (2015).
106. Hirschi, M. et al. Cryo-electron microscopy structure of the lysosomal calcium-permeable channel TRPML3. *Nature* **550**, 411–414 (2017).
107. Guo, J. et al. Structures of the calcium-activated, non-selective cation channel TRPM4. *Nature* **552**, 205–209 (2017).
108. Ge, J. et al. Architecture of the mammalian mechanosensitive Piezo1 channel. *Nature* **527**, 64–69 (2015).
109. Yan, Z. et al. Structure of the rabbit ryanodine receptor RyR1 at near-atomic resolution. *Nature* **517**, 50–55 (2015).
110. des Georges, A. et al. Structural basis for gating and activation of RyR1. *Cell* **167**, 145–157 e117 (2016).
111. Liang, Y. L. et al. Phase-plate cryo-EM structure of a class B GPCR-G-protein complex. *Nature* **546**, 118–123 (2017).
112. Zhang, Y. et al. Cryo-EM structure of the activated GLP-1 receptor in complex with a G protein. *Nature* **546**, 248–253 (2017).
113. Liang, Y. L. et al. Phase-plate cryo-EM structure of a biased agonist-bound human GLP-1 receptor-Gs complex. *Nature* **555**, 121–125 (2018).
114. García-Nafraía, J., Lee, Y., Bai, X., Carpenter, B. & Tate, C. G. Cryo-EM structure of the adenosine A2A receptor coupled to an engineered heterotrimeric G protein. *bioRxiv* <https://doi.org/10.1101/267674> (2018).
115. Carpenter, B., Nehme, R., Warne, T., Leslie, A. G. & Tate, C. G. Structure of the adenosine A<sub>2A</sub> receptor bound to an engineered G protein. *Nature* **536**, 104–107 (2016).
116. Johnson, Z. L. & Chen, J. Structural basis of substrate recognition by the multidrug resistance protein MRP1. *Cell* **168**, 1075–1085 e1079 (2017).
117. Fitzpatrick, A. W. P. et al. Cryo-EM structures of tau filaments from Alzheimer's disease. *Nature* **547**, 185–190 (2017).
118. Gremer, L. et al. Fibril structure of amyloid-beta(1–42) by cryo-electron microscopy. *Science* **358**, 116–119 (2017).
119. Kellogg, E. H. et al. Insights into the distinct mechanisms of action of taxane and non-taxane microtubule stabilizers from cryo-EM structures. *J. Mol. Biol.* **429**, 633–646 (2017).
120. Long, F. et al. Cryo-EM structures elucidate neutralizing mechanisms of anti-chikungunya human monoclonal antibodies with therapeutic activity. *Proc. Natl Acad. Sci. USA* **112**, 13898–13903 (2015).
121. Ciferri, C. et al. The trimeric serine protease HtrA1 forms a cage-like inhibition complex with an anti-HtrA1 antibody. *Biochem. J.* **472**, 169–181 (2015).
122. Lee, J. H., Ozorowski, G. & Ward, A. B. Cryo-EM structure of a native, fully glycosylated, cleaved HIV-1 envelope trimer. *Science* **351**, 1043–1048 (2016).
123. Liu, Q. et al. Quaternary contact in the initial interaction of CD4 with the HIV-1 envelope trimer. *Nat. Struct. Mol. Biol.* **24**, 370–378 (2017).
124. Wong, W. et al. Cryo-EM structure of the Plasmodium falciparum 80S ribosome bound to the anti-protozoan drug emetine. *eLife* **3**, e03080 (2014).
125. Wong, W. et al. Mefloquine targets the Plasmodium falciparum 80S ribosome to inhibit protein synthesis. *Nat. Microbiol.* **2**, 17031 (2017).
126. Khoshouei, M. et al. Volta phase plate cryo-EM of the small protein complex Prx3. *Nat. Commun.* **7**, 10534 (2016).
127. Frank, J. Advances in the field of single-particle cryo-electron microscopy over the last decade. *Nat. Protoc.* **12**, 209–212 (2017).
128. Rubinstein, J. L. Cryo-EM captures the dynamics of ion channel opening. *Cell* **168**, 341–343 (2017).
129. Stuart, D. I., Subramaniam, S. & Abrescia, N. G. The democratization of cryo-EM. *Nat. Methods* **13**, 607–608 (2016).
130. Santos, R. et al. A comprehensive map of molecular drug targets. *Nat. Rev. Drug Discov.* **16**, 19–34 (2017).
131. Hauer, F. et al. GraDeR: membrane protein complex preparation for single-particle cryo-EM. *Structure* **23**, 1769–1775 (2015).
132. Tribet, C., Audebert, R. & Popot, J. L. Amphipols: polymers that keep membrane proteins soluble in aqueous solutions. *Proc. Natl Acad. Sci. USA* **93**, 15047–15050 (1996).
133. Nath, A., Atkins, W. M. & Sligar, S. G. Applications of phospholipid bilayer nanodiscs in the study of membranes and membrane proteins. *Biochemistry* **46**, 2059–2069 (2007).
134. Tao, H. et al. Engineered nanostructured beta-sheet peptides protect membrane proteins. *Nat. Methods* **10**, 759–761 (2013).
135. Scheres, S. H. et al. Disentangling conformational states of macromolecules in 3D-EM through likelihood optimization. *Nat. Methods* **4**, 27–29 (2007).
136. Lyumkis, D., Brilot, A. F., Theobald, D. L. & Grigorieff, N. Likelihood-based classification of cryo-EM images using FREALIGN. *J. Struct. Biol.* **183**, 377–388 (2013).
137. Zhou, A. et al. Structure and conformational states of the bovine mitochondrial ATP synthase by cryo-EM. *eLife* **4**, e10180 (2015).
138. Taylor, N. M. I. et al. Structure of the human multidrug transporter ABCG2. *Nature* **546**, 504–509 (2017).
139. Oldham, M. L. et al. A mechanism of viral immune evasion revealed by cryo-EM analysis of the TAP transporter. *Nature* **529**, 537–540 (2016).
140. Karplus, P. A. & Diederichs, K. Linking crystallographic model and data quality. *Science* **336**, 1030–1033 (2012).
141. van Heel, M. & Schatz, M. Fourier shell correlation threshold criteria. *J. Struct. Biol.* **151**, 250–262 (2005).
142. Neumann, P., Dickmanns, A. & Ficner, R. Validating resolution revelation. *Structure* <https://doi.org/10.1016/j.str.2018.03.004> (2018).



143. Penczek, P. A., Grassucci, R. A. & Frank, J. The ribosome at improved resolution: new techniques for merging and orientation refinement in 3D cryo-electron microscopy of biological particles. *Ultramicroscopy* **53**, 251–270 (1994).
144. Sigworth, F. J. A maximum-likelihood approach to single-particle image refinement. *J. Struct. Biol.* **122**, 328–339 (1998).
145. Milazzo, A. C. et al. Initial evaluation of a direct detection device detector for single particle cryo-electron microscopy. *J. Struct. Biol.* **176**, 404–408 (2011).
146. Li, X. et al. Electron counting and beam-induced motion correction enable near-atomic-resolution single-particle cryo-EM. *Nat. Methods* **10**, 584–590 (2013).
147. Veesler, D. et al. Maximizing the potential of electron cryomicroscopy data collected using direct detectors. *J. Struct. Biol.* **184**, 193–202 (2013).
148. McMullan, G., Faruqi, A. R., Clare, D. & Henderson, R. Comparison of optimal performance at 300keV of three direct electron detectors for use in low dose electron microscopy. *Ultramicroscopy* **147**, 156–163 (2014).
149. Kijper, M. et al. FEI's direct electron detector developments: embarking on a revolution in cryo-TEM. *J. Struct. Biol.* **192**, 179–187 (2015).
150. De Rosier, D. J. & Klug, A. Reconstruction of three dimensional structures from electron micrographs. *Nature* **217**, 130–134 (1968).
151. Matadeen, R. et al. The *Escherichia coli* large ribosomal subunit at 7.5 Å resolution. *Structure* **7**, 1575–1583 (1999).
152. Ludtke, S. J., Chen, D. H., Song, J. L., Chuang, D. T. & Chiu, W. Seeing GroEL at 6 Å resolution by single particle electron cryomicroscopy. *Structure* **12**, 1129–1136 (2004).
153. Zhang, X. et al. Near-atomic resolution using electron cryomicroscopy and single-particle reconstruction. *Proc. Natl Acad. Sci. USA* **105**, 1867–1872 (2008).
154. Bai, X. C., Fernandez, I. S., McMullan, G. & Scheres, S. H. Ribosome structures to near-atomic resolution from thirty thousand cryo-EM particles. *eLife* **2**, e00461 (2013).
155. Fernandez, I. S. et al. Molecular architecture of a eukaryotic translational initiation complex. *Science* **342**, 1240585 (2013).
156. Fischer, N. et al. Structure of the *E. coli* ribosome-EF-Tu complex at < 3 Å resolution by Cs-corrected cryo-EM. *Nature* **520**, 567–570 (2015).
157. Jiang, J., Pentelute, B. L., Collier, R. J. & Zhou, Z. H. Atomic structure of anthrax protective antigen pore elucidates toxin translocation. *Nature* **521**, 545–549 (2015).
158. Campbell, M. G., Veesler, D., Cheng, A., Potter, C. S. & Carragher, B. 2.8 Å resolution reconstruction of the Thermoplasma acidophilum 20S proteasome using cryo-electron microscopy. *eLife* **4**, e06380 (2015).
159. Eisenberg, D. Max Perutz's achievements: how did he do it? *Protein Sci.* **3**, 1625–1628 (1994).
160. Kendrew, J. C. et al. A three-dimensional model of the myoglobin molecule obtained by x-ray analysis. *Nature* **181**, 662–666 (1958).
161. Kendrew, J. C. et al. Structure of myoglobin: a three-dimensional fourier synthesis at 2 Å resolution. *Nature* **185**, 422–427 (1960).
162. Perutz, M. F. et al. Structure of haemoglobin: a three-dimensional fourier synthesis at 5.5-Å resolution, obtained by X-ray analysis. *Nature* **185**, 416–422 (1960).
163. Adams, M. J. et al. Structure of rhombohedral 2 zinc insulin crystals. *Nature* **224**, 491 (1969).
164. Protein Data Bank. Protein Data Bank. *Nat. New Biol.* **233**, 223 (1971).
165. Collaborative Computational Project, N. The CCP4 suite: programs for protein crystallography. *Acta Crystallogr. D Biol. Crystallogr.* **50**, 760–763 (1994).
166. Ondetti, M. A., Rubin, B. & Cushman, D. W. Design of specific inhibitors of angiotensin-converting enzyme: new class of orally active antihypertensive agents. *Science* **196**, 441–444 (1977).
167. Deisenhofer, J., Epp, O., Miki, K., Huber, R. & Michel, H. Structure of the protein subunits in the photosynthetic reaction centre of *Rhodospseudomonas viridis* at 3 Å resolution. *Nature* **318**, 618–624 (1985).
168. Miller, M., Jaskolski, M., Rao, J. K., Leis, J. & Wlodawer, A. Crystal structure of a retroviral protease proves relationship to aspartic protease family. *Nature* **337**, 576–579 (1989).
169. Navia, M. A. et al. Three-dimensional structure of aspartyl protease from human immunodeficiency virus HIV-1. *Nature* **337**, 615–620 (1989).
170. Lapatto, R. et al. X-Ray analysis of HIV-1 proteinase at 2.7 Å resolution confirms structural homology among retroviral enzymes. *Nature* **342**, 299–302 (1989).
171. Wlodawer, A. et al. Conserved folding in retroviral proteases: crystal structure of a synthetic HIV-1 protease. *Science* **245**, 616–621 (1989).
172. Miller, M. et al. Structure of complex of synthetic HIV-1 protease with a substrate-based inhibitor at 2.3 Å resolution. *Science* **246**, 1149–1152 (1989).
173. Abrahams, J. P., Leslie, A. G., Lutter, R. & Walker, J. E. Structure at 2.8 Å resolution of F1-ATPase from bovine heart mitochondria. *Nature* **370**, 621–628 (1994).
174. Baldwin, J. J. et al. Thienothiopyran-2-sulfonamides: novel topically active carbonic anhydrase inhibitors for the treatment of glaucoma. *J. Med. Chem.* **32**, 2510–2513 (1989).
175. Doyle, D. A. et al. The structure of the potassium channel: molecular basis of K<sup>+</sup> conduction and selectivity. *Science* **280**, 69–77 (1998).
176. Palczewski, K. et al. Crystal structure of rhodopsin: a G protein-coupled receptor. *Science* **289**, 739–745 (2000).
177. Abola, E., Kuhn, P., Earnest, T. & Stevens, R. C. Automation of X-ray crystallography. *Nat. Struct. Biol.* **7**, S973–S977 (2000).
178. Muchmore, S. W. et al. Automated crystal mounting and data collection for protein crystallography. *Structure* **8**, R243–R246 (2000).
179. Cohen, A. E., Ellis, P. J., Miller, M. D., Deacon, A. M. & Phizackerley, R. P. An automated system to mount cryo-cooled protein crystals on a synchrotron beam line, using compact sample cassettes and a small-scale robot. *J. Appl. Crystallogr.* **35**, 720–726 (2002).
180. Beteva, A. et al. High-throughput sample handling and data collection at synchrotrons: embedding the ESRF into the high-throughput gene-to-structure pipeline. *Acta Crystallogr. D Biol. Crystallogr.* **62**, 1162–1169 (2006).
181. Cipriani, F. et al. Automation of sample mounting for macromolecular crystallography. *Acta Crystallogr. D Biol. Crystallogr.* **62**, 1251–1259 (2006).
182. Hardy, L. W. & Malikayil, A. The impact of structure-guided drug design on clinical agents. *Curr. Drug Discov.* **11**, 15–20 (2003).
183. Ben-Shem, A. et al. The structure of the eukaryotic ribosome at 3.0 Å resolution. *Science* **334**, 1524–1529 (2011).
184. Rasmussen, S. G. et al. Crystal structure of the beta2 adrenergic receptor-Gs protein complex. *Nature* **477**, 549–555 (2011).
185. Bollag, G. et al. Vemurafenib: the first drug approved for BRAF-mutant cancer. *Nat. Rev. Drug Discov.* **11**, 873–886 (2012).
186. Erlanson, D. A., Fesik, S. W., Hubbard, R. E., Jahnke, W. & Jhoti, H. Twenty years on: the impact of fragments on drug discovery. *Nat. Rev. Drug Discov.* **15**, 605–619 (2016).
187. Purcell, E. M., Torrey, H. C. & Pound, R. V. Resonance absorption by nuclear magnetic moments in a solid. *Phys. Rev.* **69**, 37–38 (1946).
188. Bloch, F., Hansen, W. W. & Packard, M. Nuclear Induction. *Phys. Rev.* **69**, 127 (1946).
189. Saunders, M., Wishnia, A. & Kirkwood, J. G. The nuclear magnetic resonance spectrum of ribonuclease. *J. Am. Chem. Soc.* **79**, 3289–3290 (1957).
190. Ernst, R. R. Sensitivity enhancement in magnetic resonance. *Adv. Magn. Reson.* **2**, 1–135 (1966).
191. Ernst, R. R. & Anderson, W. A. Application of fourier transform spectroscopy to magnetic resonance. *Rev. Sci. Instrum.* **37**, 93 (1966).
192. Jeener, J. Oral presentation. *Ampere International Summer School* (Basko Polje, 1971).
193. Aue, W. P., Bartholdi, E. & Ernst, R. R. Two-dimensional spectroscopy. Application to nuclear magnetic resonance. *J. Chem. Phys.* **64**, 2229–2246 (1976).
194. Bax, A. & Grzesiek, S. Methodological advances in protein NMR. *Acc. Chem. Res.* **26**, 131–138 (1993).
195. Williamson, M. P., Havel, T. F. & Wuthrich, K. Solution conformation of proteinase inhibitor IIA from bull seminal plasma by <sup>1</sup>H nuclear magnetic resonance and distance geometry. *J. Mol. Biol.* **182**, 295–315 (1985).
196. Oshikata, H. et al. Three-dimensional NMR spectroscopy of a protein in solution. *Nature* **332**, 374–376 (1988).
197. Vuister, G. W., Boelens, R. & Kaptein, R. Nonselective three-dimensional NMR spectroscopy. The 3D NOE-HOHAHA experiment. *J. Magn. Reson.* **80**, 176–185 (1988).
198. Shuker, S. B., Hajduk, P. J., Meadows, R. P. & Fesik, S. W. Discovering high-affinity ligands for proteins: SAR by NMR. *Science* **274**, 1531–1534 (1996).
199. Mayer, M. & Meyer, B. Characterization of ligand binding by saturation transfer difference NMR spectroscopy. *Angew. Chem. Int. Ed.* **38**, 1784–1788 (1999).
200. Hajduk, P. J. et al. NMR-based screening of proteins containing <sup>13</sup>C-labeled methyl groups. *J. Am. Chem. Soc.* **122**, 7898–7904 (2000).
201. Dalvit, C. et al. Identification of compounds with binding affinity to proteins via magnetization transfer from bulk water. *J. Biomol. NMR* **18**, 65–68 (2000).
202. Jahnke, W. Spin labels as a tool to identify and characterize protein-ligand interactions by NMR spectroscopy. *ChemBiochem* **3**, 167–173 (2002).
203. Jahnke, W. et al. NMR reporter screening for the detection of high-affinity ligands. *Angew. Chem. Int. Ed. Engl.* **41**, 3420–3423 (2002).
204. Dalvit, C., Fagerness, P. E., Hadden, D. T., Sarver, R. W. & Stockman, B. J. Fluorine-NMR experiments for high-throughput screening: theoretical aspects, practical considerations, and range of applicability. *J. Am. Chem. Soc.* **125**, 7696–7703 (2003).
205. Ludwiczek, M. L., Baminger, B. & Konrat, R. NMR probing of protein-protein interactions using reporter ligands and affinity tags. *J. Am. Chem. Soc.* **126**, 1636–1637 (2004).
206. Bruker. Bruker Introduces SampleXpress(TM), a New and Easy-to-Use Autosampler that Delivers Increased Efficiency for NMR. Bruker <http://ir.bruker.com/investors/press-releases/press-release-details/2010/Bruker-Introduces-SampleXpressTM-a-New-and-Easy-to-Use-Autosampler-that-Delivers-Increased-Efficiency-for-NMR/default.aspx> (2010).
207. Dubochet, J. et al. Cryo-electron microscopy of vitrified specimens. *Q. Rev. Biophys.* **21**, 129–228 (1988).
208. Henderson, R. et al. Model for the structure of bacteriorhodopsin based on high-resolution electron cryomicroscopy. *J. Mol. Biol.* **213**, 899–929 (1990).
209. Henderson, R. The potential and limitations of neutrons, electrons and X-rays for atomic resolution microscopy of unstained biological molecules. *Q. Rev. Biophys.* **28**, 171–193 (1995).
210. Grigorieff, N., Ceska, T. A., Downing, K. H., Baldwin, J. M. & Henderson, R. Electron crystallographic refinement of the structure of bacteriorhodopsin. *J. Mol. Biol.* **259**, 393–421 (1996).
211. Tagari, M., Newman, R., Chagoyen, M., Carazo, J. M. & Henrick, K. New electron microscopy database and deposition system. *Trends Biochem. Sci.* **27**, 589 (2002).
212. Gonen, T. et al. Lipid-protein interactions in double-layered two-dimensional AQP0 crystals. *Nature* **438**, 633–638 (2005).
213. Jiang, W. et al. Backbone structure of the infectious epsilon15 virus capsid revealed by electron cryomicroscopy. *Nature* **451**, 1130–1134 (2008).
214. Yu, X., Jin, L. & Zhou, Z. H. 3.88 Å structure of cytoplasmic polyhedrosis virus by cryo-electron microscopy. *Nature* **453**, 415–419 (2008).
215. Community Research and Development Information Service. High-throughput three-dimensional electron microscopy. *CORDIS* [https://cordis.europa.eu/project/rcn/78402\\_en.html](https://cordis.europa.eu/project/rcn/78402_en.html) (2009).
216. Ludtke, S. J. et al. De novo backbone trace of GroEL from single particle electron cryomicroscopy. *Structure* **16**, 441–448 (2008).
217. Wood, C. et al. Collaborative computational project for electron cryo-microscopy. *Acta Crystallogr. D Biol. Crystallogr.* **71**, 123–126 (2015).
218. Beck, F. et al. Near-atomic resolution structural model of the yeast 26S proteasome. *Proc. Natl Acad. Sci. USA* **109**, 14870–14875 (2012).
219. Allegretti, M., Mills, D. J., McMullan, G., Kuhlbrandt, W. & Vonck, J. Atomic model of the F420-reducing [NiFe] hydrogenase by electron cryo-microscopy using a direct electron detector. *eLife* **3**, e01963 (2014).
220. Amunts, A. et al. Structure of the yeast mitochondrial large ribosomal subunit. *Science* **343**, 1485–1489 (2014).
221. Plaschka, C. et al. Transcription initiation complex structures elucidate DNA opening. *Nature* **533**, 353–358 (2016).
222. He, Y. et al. Near-atomic resolution visualization of human transcription promoter opening. *Nature* **533**, 359–365 (2016).

223. Tsai, K. L. et al. Mediator structure and rearrangements required for holoenzyme formation. *Nature* **544**, 196–201 (2017).
224. Schilbach, S. et al. Structures of transcription pre-initiation complex with TFIIB and Mediator. *Nature* **551**, 204–209 (2017).
225. Nguyen, T. H. D. et al. Cryo-EM structure of the yeast U4/U6. U5 tri-snRNP at 3.7 Å resolution. *Nature* **530**, 298–302 (2016).
226. Agafonov, D. E. et al. Molecular architecture of the human U4/U6. U5 tri-snRNP. *Science* **351**, 1416–1420 (2016).
227. Yan, C. et al. Structure of a yeast spliceosome at 3.6-angstrom resolution. *Science* **349**, 1182–1191 (2015).
228. Plaschka, C., Lin, P. C. & Nagai, K. Structure of a pre-catalytic spliceosome. *Nature* **546**, 617–621 (2017).
229. Yan, C., Wan, R., Bai, R., Huang, G. & Shi, Y. Structure of a yeast activated spliceosome at 3.5 Å resolution. *Science* **353**, 904–911 (2016).
230. Rauhut, R. et al. Molecular architecture of the *Saccharomyces cerevisiae* activated spliceosome. *Science* **353**, 1399–1405 (2016).
231. Galej, W. P. et al. Cryo-EM structure of the spliceosome immediately after branching. *Nature* **537**, 197–201 (2016).
232. Wan, R., Yan, C., Bai, R., Huang, G. & Shi, Y. Structure of a yeast catalytic step I spliceosome at 3.4 Å resolution. *Science* **353**, 895–904 (2016).
233. Zhang, X. et al. An atomic structure of the human spliceosome. *Cell* **169**, 918–929 e914 (2017).
234. Bertram, K. et al. Cryo-EM structure of a human spliceosome activated for step 2 of splicing. *Nature* **542**, 318–323 (2017).
235. Yan, C., Wan, R., Bai, R., Huang, G. & Shi, Y. Structure of a yeast step II catalytically activated spliceosome. *Science* **355**, 149–155 (2017).
236. Fica, S. M. et al. Structure of a spliceosome remodelled for exon ligation. *Nature* **542**, 377–380 (2017).
237. Wilkinson, M. E. et al. Postcatalytic spliceosome structure reveals mechanism of 3'-splice site selection. *Science* **358**, 1283–1288 (2017).
238. Liu, S. et al. Structure of the yeast spliceosomal postcatalytic P complex. *Science* **358**, 1278–1283 (2017).
239. Sirohi, D. et al. The 3.8 Å resolution cryo-EM structure of Zika virus. *Science* **352**, 467–470 (2016).
240. Yuan, S. et al. Cryo-EM structure of a herpesvirus capsid at 3.1 Å. *Science* **360**, eaao7283 (2018).
241. von der Ecken, J., Heissler, S. M., Pathan-Chhatbar, S., Manstein, D. J. & Raunser, S. Cryo-EM structure of a human cytoplasmic actomyosin complex at near-atomic resolution. *Nature* **534**, 724–728 (2016).
242. Ballandras-Colas, A. et al. Cryo-EM reveals a novel octameric integrase structure for betaretroviral intasome function. *Nature* **530**, 358–361 (2016).
243. Wu, M., Gu, J., Guo, R., Huang, Y. & Yang, M. Structure of mammalian respiratory supercomplex I1III2IV1. *Cell* **167**, 1598–1609 e1510 (2016).
244. Guo, R., Zong, S., Wu, M., Gu, J. & Yang, M. Architecture of human mitochondrial respiratory megacomplex I2III2IV2. *Cell* **170**, 1247–1257 e1212 (2017).
245. Gristick, H. B. et al. Natively glycosylated HIV-1 Env structure reveals new mode for antibody recognition of the CD4-binding site. *Nat. Struct. Mol. Biol.* **23**, 906–915 (2016).
246. Dambacher, C. M., Worden, E. J., Herzik, M. A., Martin, A. & Lander, G. C. Atomic structure of the 26S proteasome lid reveals the mechanism of deubiquitinase inhibition. *eLife* **5**, e13027 (2016).
247. Luan, B. et al. Structure of an endogenous yeast 26S proteasome reveals two major conformational states. *Proc. Natl Acad. Sci. USA* **113**, 2642–2647 (2016).
248. Huang, X., Luan, B., Wu, J. & Shi, Y. An atomic structure of the human 26S proteasome. *Nat. Struct. Mol. Biol.* **23**, 778–785 (2016).
249. Fischer, N. et al. The pathway to GTPase activation of elongation factor SelB on the ribosome. *Nature* **540**, 80–85 (2016).
250. Natchiar, S. K., Myasnikov, A. G., Kratzat, H., Hazemann, I. & Klaholz, B. P. Visualization of chemical modifications in the human 80S ribosome structure. *Nature* **551**, 472–477 (2017).
251. Barandun, J. et al. The complete structure of the small-subunit processome. *Nat. Struct. Mol. Biol.* **24**, 944–953 (2017).
252. Cheng, J., Kellner, N., Berninghausen, O., Hurt, E. & Beckmann, R. 3.2-Å-resolution structure of the 90S preribosome before A1 pre-rRNA cleavage. *Nat. Struct. Mol. Biol.* **24**, 954–964 (2017).
253. Sanghai, Z. A. et al. Modular assembly of the nucleolar pre-60S ribosomal subunit. *Nature* **556**, 126–129 (2018).
254. Zhang, R., Alushin, G. M., Brown, A. & Nogales, E. Mechanistic origin of microtubule dynamic instability and its modulation by EB proteins. *Cell* **162**, 849–859 (2015).
255. Passos, D. O. et al. Cryo-EM structures and atomic model of the HIV-1 strand transfer complex intasome. *Science* **355**, 89–92 (2017).
256. Bednar, J. et al. Structure and dynamics of a 197 bp nucleosome in complex with linker histone H1. *Mol. Cell* **66**, 384–397 e8 (2017).
257. Ilangovan, A. et al. Cryo-EM structure of a relaxase reveals the molecular basis of DNA unwinding during bacterial conjugation. *Cell* **169**, 708–721 e12 (2017).
258. Chowdhury, S. et al. Structure reveals mechanisms of viral suppressors that intercept a CRISPR RNA-guided surveillance complex. *Cell* **169**, 47–57 e11 (2017).
259. Guo, T. W. et al. Cryo-EM structures reveal mechanism and inhibition of DNA targeting by a CRISPR-Cas surveillance complex. *Cell* **171**, 414–426 e12 (2017).
260. Brown, A. et al. Structures of the human mitochondrial ribosome in native states of assembly. *Nat. Struct. Mol. Biol.* **24**, 866–869 (2017).
261. Casanál, A. et al. Architecture of eukaryotic mRNA 3'-end processing machinery. *Science* **358**, 1056–1059 (2017).
262. Clerici, M., Faini, M., Muckenfuss, L. M., Aebersold, R. & Jinek, M. Structural basis of AAUAAA polyadenylation signal recognition by the human CPSF complex. *Nat. Struct. Mol. Biol.* **25**, 135–138 (2018).
263. Urnavicius, L. et al. Cryo-EM shows how dynactin recruits two dyneins for faster movement. *Nature* **554**, 202–206 (2018).
264. Poepsel, S., Kasinath, V. & Nogales, E. Cryo-EM structures of PRC2 simultaneously engaged with two functionally distinct nucleosomes. *Nat. Struct. Mol. Biol.* **25**, 154–162 (2018).
265. Bai, L., Wang, T., Zhao, G., Kovach, A. & Li, H. The atomic structure of a eukaryotic oligosaccharyltransferase complex. *Nature* **555**, 328–333 (2018).
266. Shen, K. et al. Architecture of the human GATOR1 and GATOR1-Rag GTPases complexes. *Nature* **556**, 64–69 (2018).
267. Zyryanova, A. F. et al. Binding of ISRIB reveals a regulatory site in the nucleotide exchange factor eIF2B. *Science* **359**, 1533–1536 (2018).
268. Scapin, G. et al. Structure of the insulin receptor-insulin complex by single-particle cryo-EM analysis. *Nature* **556**, 122–125 (2018).
269. Meyerson, J. R. et al. Structural basis of kainate subtype glutamate receptor desensitization. *Nature* **537**, 567–571 (2016).
270. Matthies, D. et al. Cryo-EM structures of the magnesium channel CorA reveal symmetry break upon gating. *Cell* **164**, 747–756 (2016).
271. Whichee, J. R. & MacKinnon, R. Structure of the voltage-gated K(+) channel Eag1 reveals an alternative voltage-sensing mechanism. *Science* **353**, 664–669 (2016).
272. Tao, X., Hite, R. K. & MacKinnon, R. Cryo-EM structure of the open high-conductance Ca<sup>2+</sup>-activated K<sup>+</sup> channel. *Nature* **541**, 46–51 (2017).
273. Li, M. et al. Structure of a eukaryotic cyclic-nucleotide-gated channel. *Nature* **542**, 60–65 (2017).
274. Lee, C. H. & MacKinnon, R. Structures of the human HCN1 hyperpolarization-activated channel. *Cell* **168**, 111–120 e111 (2017).
275. Basak, S. et al. Cryo-EM structure of 5-HT3A receptor in its resting conformation. *Nat. Commun.* **9**, 514 (2018).
276. Zhang, Z. & Chen, J. Atomic structure of the cystic fibrosis transmembrane conductance regulator. *Cell* **167**, 1586–1597 e1589 (2016).
277. Lu, W., Du, J., Goehring, A. & Gouaux, E. Cryo-EM structures of the trimeric NMDA receptor and its allosteric modulation. *Science* **355**, eaal3729 (2017).
278. Wang, W. & MacKinnon, R. Cryo-EM structure of the open human ether-a-go-go-related K<sup>+</sup> channel hERG. *Cell* **169**, 422–430 e410 (2017).
279. Jackson, S. M. et al. Structural basis of small-molecule inhibition of human multidrug transporter ABCG2. *Nat. Struct. Mol. Biol.* **25**, 333–340 (2018).
280. Schmiege, P., Fine, M., Blobel, G. & Li, X. Human TRPML1 channel structures in open and closed conformations. *Nature* **550**, 366–370 (2017).
281. Chen, Q. et al. Structure of mammalian endolysosomal TRPML1 channel in nanodiscs. *Nature* **550**, 415–418 (2017).
282. Winkler, P. A., Huang, Y., Sun, W., Du, J. & Lu, W. Electron cryo-microscopy structure of a human TRPM4 channel. *Nature* **552**, 200–204 (2017).
283. Martin, G. M., Kandasamy, B., DiMaio, F., Yoshioka, C. & Shyng, S. L. Anti-diabetic drug binding site in a mammalian KATP channel revealed by Cryo-EM. *eLife* **6**, e31054 (2017).
284. Zubcevic, L. et al. Cryo-electron microscopy structure of the TRPV2 ion channel. *Nat. Struct. Mol. Biol.* **23**, 180–186 (2016).
285. Deng, Z. et al. Cryo-EM and X-ray structures of TRPV4 reveal insight into ion permeation and gating mechanisms. *Nat. Struct. Mol. Biol.* **25**, 252–260 (2018).
286. Hughes, T. E. T. et al. Structural basis of TRPV5 channel inhibition by econazole revealed by cryo-EM. *Nat. Struct. Mol. Biol.* **25**, 53–60 (2018).
287. Shen, P. S. et al. The structure of the polycystic kidney disease channel PKD2 in lipid nanodiscs. *Cell* **167**, 763–773 e111 (2016).
288. Roh, S. H. et al. The 3.5-Å CryoEM structure of nanodisc-reconstituted yeast vacuolar ATPase Vo proton channel. *Mol. Cell* **69**, 993–1004 e1003 (2018).
289. She, J. et al. Structural insights into the voltage and phospholipid activation of the mammalian TPC1 channel. *Nature* **556**, 130–134 (2018).
290. Qian, P., Siebert, C. A., Wang, P., Canniffe, D. P. & Hunter, C. N. Cryo-EM structure of the Blastochloris viridis LH1-RC complex at 2.9 Å. *Nature* **556**, 203–208 (2018).
291. Sun, C. et al. Structure of the alternative complex III in a supercomplex with cytochrome oxidase. *Nature* **557**, 123–126 (2018).
292. Ruan, J., Xia, S., Liu, X., Lieberman, J. & Wu, H. Cryo-EM structure of the gasdermin A3 membrane pore. *Nature* **557**, 62–67 (2018).
293. Chua, E. Y. et al. 3.9 Å structure of the nucleosome core particle determined by phase-plate cryo-EM. *Nucleic Acids Res.* **44**, 8013–8019 (2016).
294. Xie, Q. et al. The 2.8 Å electron microscopy structure of adeno-associated virus-DJ bound by a heparinoid pentasaccharide. *Mol. Ther. Methods Clin. Dev.* **5**, 1–12 (2017).
295. Shalev-Benami, M. et al. Atomic resolution snapshot of Leishmania ribosome inhibition by the aminoglycoside paromomycin. *Nat. Commun.* **8**, 1589 (2017).
296. Liu, Z. et al. Structure and assembly model for the Trypanosoma cruzi 60S ribosomal subunit. *Proc. Natl Acad. Sci. USA* **113**, 12174–12179 (2016).
297. Liu, Z. et al. Determination of the ribosome structure to a resolution of 2.5 Å by single-particle cryo-EM. *Protein Sci.* **26**, 82–92 (2017).
298. Banerjee, S. et al. 2.3 Å resolution cryo-EM structure of human p97 and mechanism of allosteric inhibition. *Science* **351**, 871–875 (2016).
299. Dong, Y. et al. Antibody-induced uncoating of human rhinovirus B14. *Proc. Natl Acad. Sci. USA* **114**, 8017–8022 (2017).
300. Golas, M. M. et al. Snapshots of the RNA editing machine in trypanosomes captured at different assembly stages in vivo. *EMBO J.* **28**, 766–778 (2009).
301. Sander, B., Golas, M. M., Lührmann, R. & Stark, H. An approach for de novo structure determination of dynamic molecular assemblies by electron cryomicroscopy. *Structure* **18**, 667–676 (2010).
302. Tsai, J. C. et al. Structure of the nucleotide exchange factor eIF2B reveals mechanism of memory-enhancing molecule. *Science* **359**, eaa0939 (2018).

## Competing interests

The authors declare competing interests: see Web version for details.

## Publisher's note

Springer Nature remains neutral with regard to jurisdictional claims in published maps and institutional affiliations.

## RELATED LINKS

EPU (Thermo Fisher Scientific automated data acquisition software for single-particle analysis workflow): <https://www.fei.com/software/eipu/>

JADAS (JEOL Automated Data Acquisition System): <https://www.jeolusa.com/PRODUCTS/Transmission-Electron-Microscopes-TEM/Analytical-Data-Optimization/Automated-Data-Acquisition-JADAS>

Thermo Fisher Scientific Glacios: <https://www.fei.com/glacios/>

XChem framework at the Diamond synchrotron: <http://www.diamond.ac.uk/Beamlines/Mx/Fragment-Screening.html>

ALL LINKS ARE ACTIVE IN THE ONLINE PDF